Fast finite element modelling of bridled leading-edge inflatable kites

P.I.H. Roeleveld

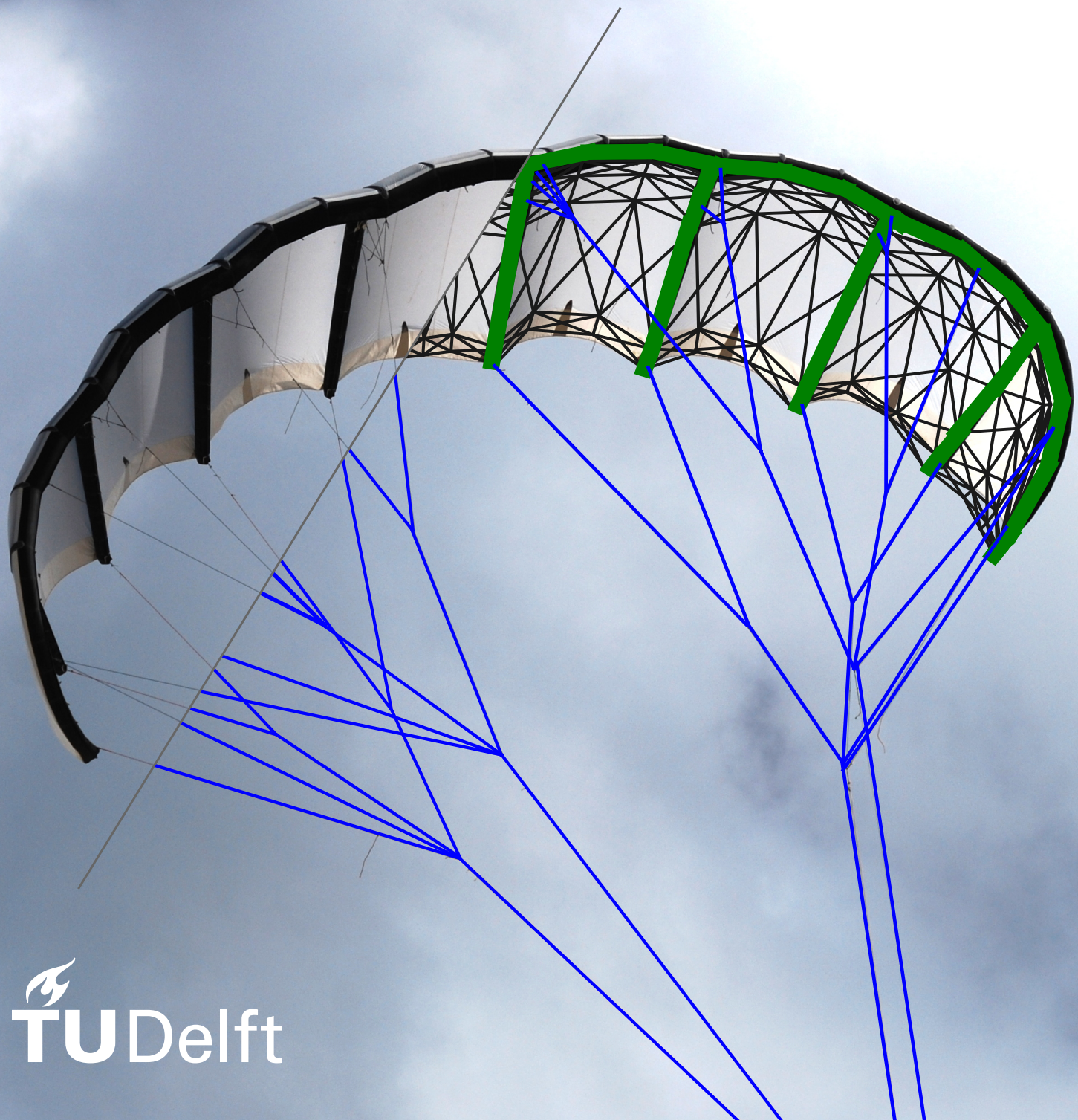

Delft University of Technology

TU Delft

Fast finite element modelling of bridled leading-edge inflatable kites

by

P.I.H. Roeleveld

To obtain the degree of Master of Science in Aerospace Engineering
at the Delft University of Technology.

Student number:	4754781	
Project duration:	March 3, 2025 - March 4, 2026	
Thesis comittee:	Dr. ir. F. de Prenter	Chair
	Dr.-Ing. S.G.P. Castro	Examiner
	Dr.-Ing. R. Schmehl	Responsible supervisor
	Ir. J.A.W. Poland	Daily supervisor

Cover: TU Delft V3 kite with overlaid finite element model

TU Delft

Contents

List of Figures

List of Tables

Nomenclature

Abbreviations

Abbreviation	Definition
AWE	Airborne wind energy
CAD	Computer aided design
CFD	Computational fluid dynamics
DOF	Degrees of freedom
FEM	Finite element model
FSI	Fluid-structure interaction
LC	Load case
LEI	Leading edge inflatable
PSM	Particle System model
VSM	Vortex step method

Symbols

Symbol	Definition	Unit
Matrices		
$\mathbf{C}$	Damping matrix	$\mathrm{kg\,s^{-1}}$
$\mathbf{I}$	Identity matrix	$-$
$\mathbf{K}$	Stiffness matrix	$\mathrm{N\,m^{-1}}$
$\mathbf{M}$	Mass matrix	kg
$\mathbf{R}$	Rotation matrix	$-$
$\mathbf{T}$	Coordinate system rotation matrix	$-$
Vectors		
$\mathbf{f}$	Force vector	N
$\mathbf{r}$	Residual force vector	N
$\mathbf{u}$	Displacement vector	m
$\dot{\mathbf{u}}$	Velocity vector	$\mathrm{ms^{-1}}$
$\ddot{\mathbf{u}}$	Acceleration vector	$\mathrm{ms^{-2}}$
$\mathbf{v}_{xy}$	Vector on the xy plane	m
$\mathbf{x}$	Vector in x direction	m
$\mathbf{y}$	Vector in y direction	m
$\mathbf{z}$	Vector in z direction	m
Latin		
A	Area	$\mathrm{m^2}$
B	Camera distance	m
c	Identity stiffness constant	$\mathrm{N\,m^{-1}}$
C	Breukels' equation constant	$-$
d	Diameter	m
E	Young's modulus	Pa
G	Shear modulus	Pa
I	Area moment of inertia	$\mathrm{m^4}$
k	Shear correction factor	$-$
k_x	Spring stiffness	$\mathrm{N\,m^{-1}}$
L	Length	m
L_0	Rest length	m
m	mass	$-$
n	Node	$-$
p	Pressure	Pa
P	Tip load	N
r	Radius	m
S_v	Deflection scaling factor	$-$
S_φ	Rotation scaling factor	$-$
T	Torque	$\mathrm{N\,m}$
u	Deflection in x direction	m
v	Deflection in y direction	m
w	Deflection in z direction	m
x	Coordinate in x direction	m
y	Coordinate in x direction	m
z	Coordinate in x direction	m

Greek		
ϵ	Error	m
ε	Relative error	$\%$
ρ_l	Line density	$\mathrm{kg\,m^{-1}}$
ρ_A	Area density	$\mathrm{kg\,m^{-2}}$
ρ	density	$\mathrm{kg\,m^{-3}}$
φ	Deflection angle along x axis	rad
θ	Deflection angle along y axis	rad
ψ	Deflection angle along z axis	rad
Θ	Camera angle	rad

Preface

This work is the cumulation of my academic journey in Delft, starting in 2017. As a bachelor student, I was always intrigued by renewable energies, which led me to pursue the master track Aerodynamics and Wind Energy. Here, I followed the course on airborne wind energy, given by Roland. I was immediately very interested in the topic and was enthusiastic when I heard that thesis opportunities were available in this field. I contacted Jelle last year and he had several proposals for a thesis subject. I chose to work on the structural modelling of a kite, which was something that I had no prior experience with. The experience was challenging but rewarding, and I am proud of the end result.

I would like to thank Jelle Poland for his daily supervision, your enthusiasm and expertise always provided very helpful throughout the thesis. Furthermore I would like to thank Roland Schmehl for his supervision as well, I am very glad that we were able to have weekly update meetings, the sessions together with Roland and Jelle always provided a lot of input and guidance. I would also like to thank Saullo Castro for his involvement, having provided the pyfe3d codebase used as a basis of this thesis and providing help whenever me, Roland and Jelle were unsure on how to continue. I also want to thank Pim Haanen, for helping me obtain the validation data for the hanging kite case.

On a more personal note I would like thank my parents Bert and Els for raising me and always believing in me, and their continued interest into my work. A special thanks goes to my girlfriend Noor who has supported me this past year and has probably listened to me talk about kites for way too long already, so much so that we both started taking up kitesurfing. Lastly, I would like to thank all the friends I made along the way during my time in Delft, you made my time in Delft unforgettable.

P.I.H. Roeleveld
Delft, February 2026

Abstract

Leading-edge inflatable (LEI) kites are used in airborne wind energy (AWE) systems. Accurate prediction of their aero-structural behaviour is essential for reliable performance estimation, control system development, and the design of scalable AWE systems. Modelling LEI kites remains challenging due to strong aero–structural interaction. Existing structural modelling approaches often face a trade-off between computational efficiency and physical fidelity, particularly when representing the bending and torsional stiffness of inflatable beams. Models either overly simplify the complex bridle line system, or simplify the wing of the kite. A uniform approach is desired, where both can be modelled in detail while remaining computationally efficient.

This thesis presents a computationally efficient structural modelling approach that captures the bending and torsional behaviour of the inflatable leading edge and struts of an LEI kite for use within a partitioned aero-structural simulation framework. Two candidate modelling approaches are investigated: a particle system model (PSM and a reduced geometrically non-linear finite element model (FEM). A comparative study based on a cantilevered beam configuration demonstrates that, while particle-based representations can reproduce beam bending behaviour, they require a high level amount of degrees of freedom (DOF) to achieve sufficient accuracy, resulting in increased computational cost and reduced numerical robustness. In contrast, a finite element formulation employing beam elements achieves good accuracy with substantially fewer DOF.

Based on this analysis, a dedicated FEM framework is developed to model the structural behaviour of a bridled LEI kite. The model employs a co-rotational formulation to account for large displacements and rotations, required for resolving the bridle line system. The framework is built on two-node finite elements, and the system is solved using the Newton-Raphson iteration scheme. Kite-specific structural elements are introduced to represent the inflatable beams, the bridle line system, and the canopy. The various elements are independently verified. The approach to coupling the structural to an aerodynamic model using a quasi-steady, partitioned aero–structural approach, is discussed.

The developed FEM is applied to the TU Delft V3 kite and validated against static hanging-test measurements for multiple load cases and internal pressures. The simulations show good agreement with experimental data in terms of global deformations and characteristic lengths, like the span and trailing edge length. The model successfully captures the effect of canopy billowing. Compared to the previously used PSM, the proposed approach provides a significant improvement in deformation resolution while remaining suitable for iterative aero-structural simulations.

The presented modelling framework bridges the gap between low-fidelity structural representations and computationally expensive membrane-based models. It enables improved aero-structural analysis of LEI kites and forms a basis for future work on aero-structural interaction, control-oriented modelling, and the design and optimisation of large-scale airborne wind energy systems.

1

Introduction

The airborne wind energy (AWE) sector seeks to make wind energy available at a lower material cost by harvesting wind energy using kites [40]. A large part of the sector is dedicated to producing wind power with crosswind pumping cycles using soft-wing kites. The crosswind kite power concept was first proposed by Loyd [28]. A pumping cycle consists of a reel-out, generating energy, and a reel-in phase, consuming energy [50]. Flying the kite crosswind during reel-out and depowering the kite during reel-in leads to a net energy gain over the pumping cycle. During reel-out the kite is deformed to steer into the prescribed pattern. Between reel-in and reel-out the kite transitions from a powered and depowered state. These deformations are induced by pulling or loosening the bridle lines, which define the aerodynamic shape of the wing. Furthermore the kite is steered by pulling on steering lines, also deforming the wing. The kite can therefore be considered as a morphing aerodynamic control surface [36]. The cycle is visualised in Figure 1.1. With the upscaling of kites from $10\ \mathrm{m}^2$ to surface areas up to $500\ \mathrm{m}^2$, reliance on computational methods for kites has increased. Conventional kite design methods rely on experimental testing, but this method has become too expensive, time-consuming, and risky for AWE applications [6].

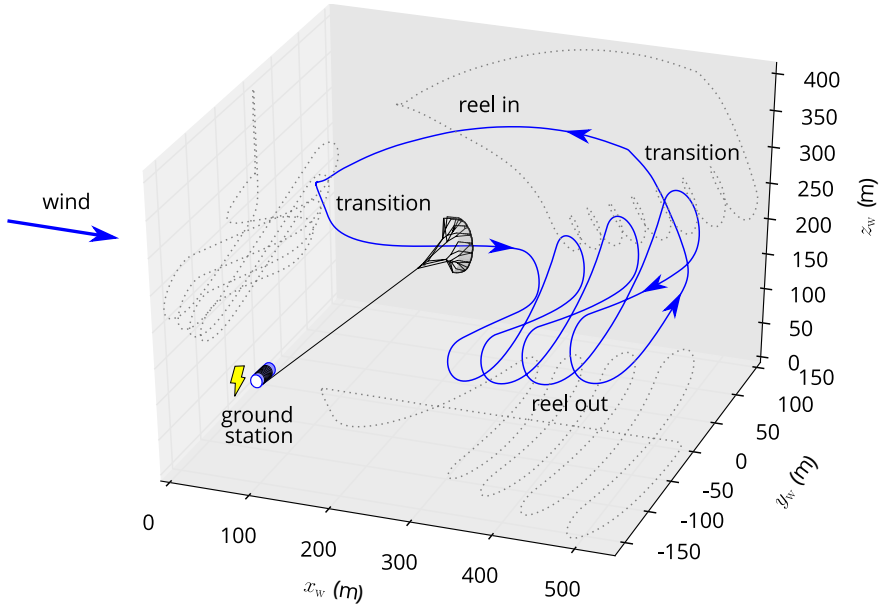

Figure 1.1: Visualisation of the pumping cycle of a leading-edge inflatable kite [40]

At the Delft University of Technology, research of AWE systems has led to a variety of kites developed specifically for wind energy applications. The developed kites are soft-wing leading-edge inflatable (LEI) kites similar to those used in kitesurfing applications, but with a larger surface area. The LEI Kite uses an inflatable beam along the leading edge and several smaller beams, called struts, along the wing's chord to define the structure's shape. Furthermore a LEI kite makes use of a bridle line system, consisting of knots lines and pulleys to further constrain the wing's shape. The TU Delft V3 kite, has been used extensively in literature. Its data is open-source available, including computer aided design (CAD) files, computational fluid dynamics (CFD) analysis, flight tests, and much more [35]. The kite can be seen in Figure 1.2a, and characteristic properties of the kite are presented in Table 1.1.

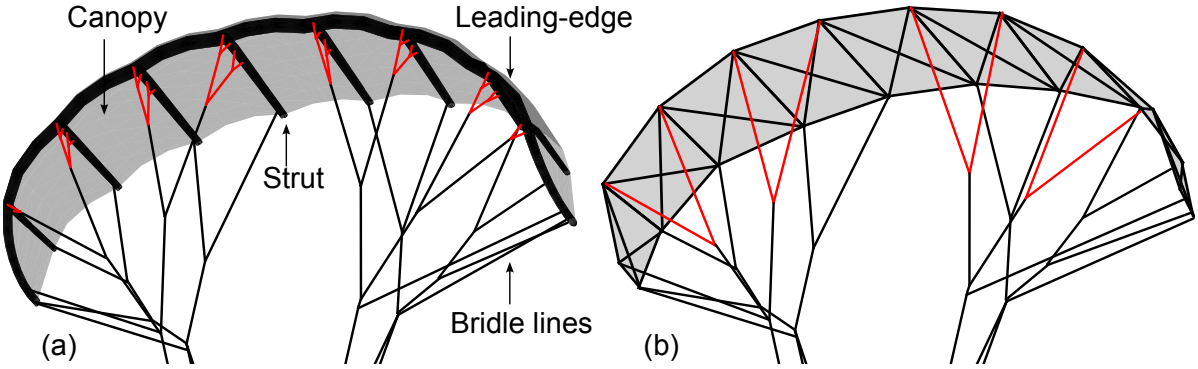

Figure 1.2: (a) CAD Geometry of the TU Delft V3 Kite including bridle lines, where red lines indicate bridles that are simplified in the particle system model (b) Particle system model of the TU Delft V3 kite with a simplified bridle system and no inflatable leading-edge or struts, with red lines indicating simplifications made compared to the full bridle line system [36].

Table 1.1: Properties of the TU Delft V3 Kite [35], dimensions are taken from CAD geometry data

Property	Unit	Value	Property	Unit	Value
Flat area	(m^2)	25	CoG wing in x-dir.	$(\%)$	54
Number of struts	$(-)$	8	CoG wing in z-dir.	$(\%)$	34
Flat wing span	(m)	11	Ixx wing	(kgm^2)	85
Flat maximum chord	(m)	2.6	Iyy wing	(kgm^2)	13
Flat aspect ratio	$(-)$	5	Izz wing	(kgm^2)	83
Projected area	(m^2)	20	Ixz wing	(kgm^2)	-0.66
Projected wing span	(m)	8.3	Bridle height	(m)	9.6
Projected wing height	(m)	3.1	Number of bridle lines	$(-)$	82
Projected aspect ratio	$(-)$	3.5	Total length bridle lines	(m)	96
Side view area	(m^2)	5.6	Number of pulleys in bridle	$(-)$	20
Leading edge 3D length	(m)	11	Unbridled mass	(kg)	11
Trailing edge 3D length	(m)	11	Nominal pulling force	(kN)	5.8

Simulating a kite in flight is computationally expensive, due to the strong aero-structural coupling. Therefore, there is a desire for structural models that are both simple, to reduce computations, and accurate, to capture the physics and deformation of the kite. Structural models of kites reported in the literature that can capture deformation often rely on commercial software, require calibration of parameters, or lack robustness [4, 6]. Poland and Schmehl [36] developed a structural model specifically for aero-structural coupled problems. The model is based on lumped mass particles connected by spring-damper elements. Such a particle

system model (PSM) is well-suited as a structural model for a soft-wing kite because it can resolve the bridle line system, which dominates the shape of a soft-wing kite [36]. The model enforces the canopy into quadrilateral sections where each corner is connected to the others with a spring.

One limitation of the PSM lies in its treatment of the bridle line system. In the physical V3 kite, the bridle lines attach at multiple points along the wing chord. The spring-damper elements can transmit tensile and compressive forces, but lack rotational resistance at the connection points. Therefore, the bridle lines can only be introduced at the strut's endpoints. Attempting to represent additional attachment points by introducing multiple spring-damper elements along the chord produces a non-physical response. To address this, the bridle line system was adapted. Fig. 1.2(a) shows the physical V3 kite, whereas Fig. 1.2(b) shows the adapted kite for the PSM. This simplification can be resolved by including the bending stiffness of the leading edge and struts. However, including bending stiffness in a PSM can come at a significant computational cost [21]. This thesis seeks to include the bending stiffness of the kite's inflatable structure into a structural model. The structural model to be developed should be open-source, fast and sufficiently accurate.

This report focusses on the development, verification and validation of a structural kite model for use in aero-structural simulations. The report is structured as follows. Chapter 2 presents a review of the literature on structural modelling of leading-edge inflatable kites, and concludes with the formulation of the research objective and research questions. Then, Chapter 3 investigates the two most promising modelling strategies, assessing the scaleability of both to a kite and choosing a single model moving forward. After that, Chapter 4 introduces the overall aero-structural framework and describes the coupling strategy between the aerodynamic and structural solvers. Chapter 5 details the finite element modelling approach developed for LEI kites, including the treatment of geometric non-linearity and kite-specific structural components, and presents verification cases. The framework is applied to the TU Delft V3 kite in Chapter 6, and the experimental setup used for validation is described. Chapter 7 analyses the simulation results and compares the predicted deformations with experimental measurements. Then, Chapter 8 draws conclusions by answering the research questions and evaluating the modelling approach. Lastly, Chapter 9 outlines recommendations for future research and model extensions.

2

Literature review

In this chapter the literature on structural kite modelling is reviewed. First, in Section 2.1, the non-linearities apparent in kites are discussed, as these are key to resolve in a structural kite model. In Section 2.2, the approach to coupling a structural model to an aerodynamic model is discussed. Then, Section 2.3 and Section 2.4 discuss the deformations and vibrations that a kite experiences in flight. After that, Section 2.5 compiles all different types of structural models and describes their complexity and physicality. Non-linear modelling approaches used to find the static solution of a structural problem is given in Section 2.6. The approach to modelling a beam inside a particle system model and finite element model is shared in Section 2.7. Lastly, Section 2.8 shares the research objective and states the research questions to be answered in this work.

2.1. Non-linearities in kites

Modelling a kite's dynamics, aerodynamics, and deformation through simulation is difficult, as the problem is non-linear. Bosch [4] notes three sources of non-linearities in a LEI kite. Geometric non-linearities, material non-linearities, and force non-linearities are all apparent in a LEI kite and must be accounted for in a model. A detailed explanation of the three non-linearities is given.

- **Geometric non-linearity:** A kite undergoes large displacements and rotations leading to significant changes in its geometry during flight. A linear approach to structural modelling is no longer accurate in such cases, as it assumes small deformations and constant stiffness. The model needs to account for the change in structural stiffness and internal force distribution due to the change in geometry.
- **Material non-linearity:** Material non-linearities are apparent in the inflatable structures in the kite. The Young's modulus depends on the beam's deflection [6]. Material non-linearities are also evident in the membrane material, which is a woven material and a complex structure exhibiting non-linear stress-strain behaviour [46].
- **Force non-linearity:** A kite's aerodynamic load depends on its shape, which changes as the kite deforms. The external forces are not fixed and change as the structure deforms, leading to a force non-linearity. As a result, the problem becomes a fluid-structure interaction (FSI) problem, where the aerodynamics and deformation influence each other.

2.2. Aero-structural coupling

Before the AWE sector emerged, soft kites were primarily developed for kitesurfing. In the kitesurfing industry, kite design has followed a experience based design approach [6], with iterative modifications based on previous models and experimental testing. This approach is a time and resource-intensive way to develop new kites with large surface areas. Therefore, there is a desire to simulate an AWE kite's performance to iterate on the kite design before committing to developing a kite in real life.

Determining the performance of a soft-wing kite computationally is a non-trivial task. The non-linearities apparent in the kite lead to computationally expensive models. The FSI problem that emerges can be solved with two approaches. The first one is the partitioned approach, where a structural and aerodynamic model is coupled, and both outputs are set up as an input for the other and iterated upon until convergence. Alternatively, one can solve the structural deformation and aerodynamic loads in a single coupled "monolithic" solver. Both methods are visualised in Figure 2.1.

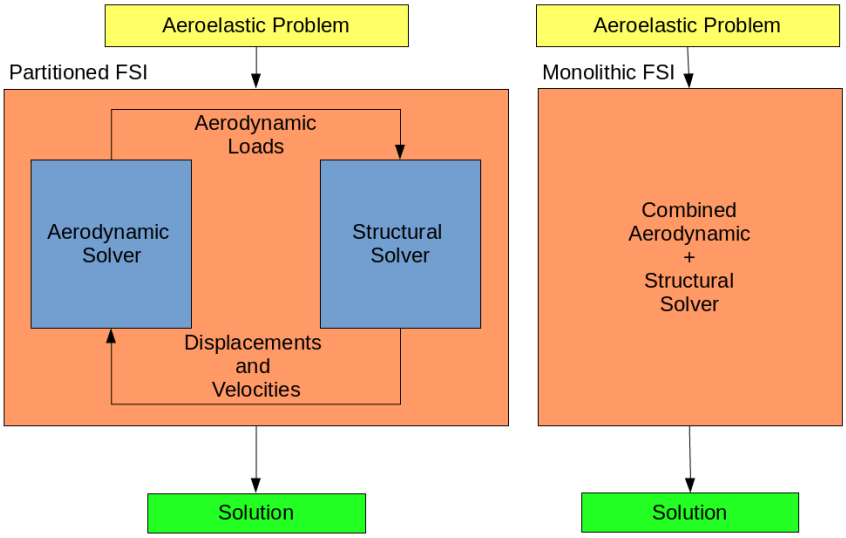

Figure 2.1: Partitioned and Monolithic FSI methods [27]

The iterative nature of a partitioned FSI solver leads to a more computationally expensive approach compared to a monolithic FSI solver. However, the setup of a monolithic FSI solver is a lot more complex and less flexible in nature. The advantage of a partitioned solver is in the freedom to vary both models and the ease of developing such models independently. Because of this, the current preference in the AWE sector is the partitioned approach. To ensure a quick convergence time, aerodynamic and structural models are chosen to be as simple as possible while capturing the desired effects.

Multiple structural models and aerodynamic solvers have previously been combined to derive a kite FSI model. Folkersma has modelled ram-air kites [13] and Thedens [46]. Notable attempts for LEI kites are as follows. Breukels [6] modelled a LEI kite by developing a structural and an aerodynamic solver. Bosch [4] developed a different structural model and coupled it to the aerodynamic solver of Breukels. Geschiere [15] adapted Bosch's structural model to include the bridle system. Berens made further improvements on this model [3]. The latest approach for LEI kites [37, 36, 8] forms the basis for this study and features a particle system model

(PSM) for the structural part and a vortex step method (VSM) model for the aerodynamics. Both models are visualized in Figure 2.2. The model is quasi-steady, which means that for a change in aerodynamic load, the static solution of the structural response is determined.

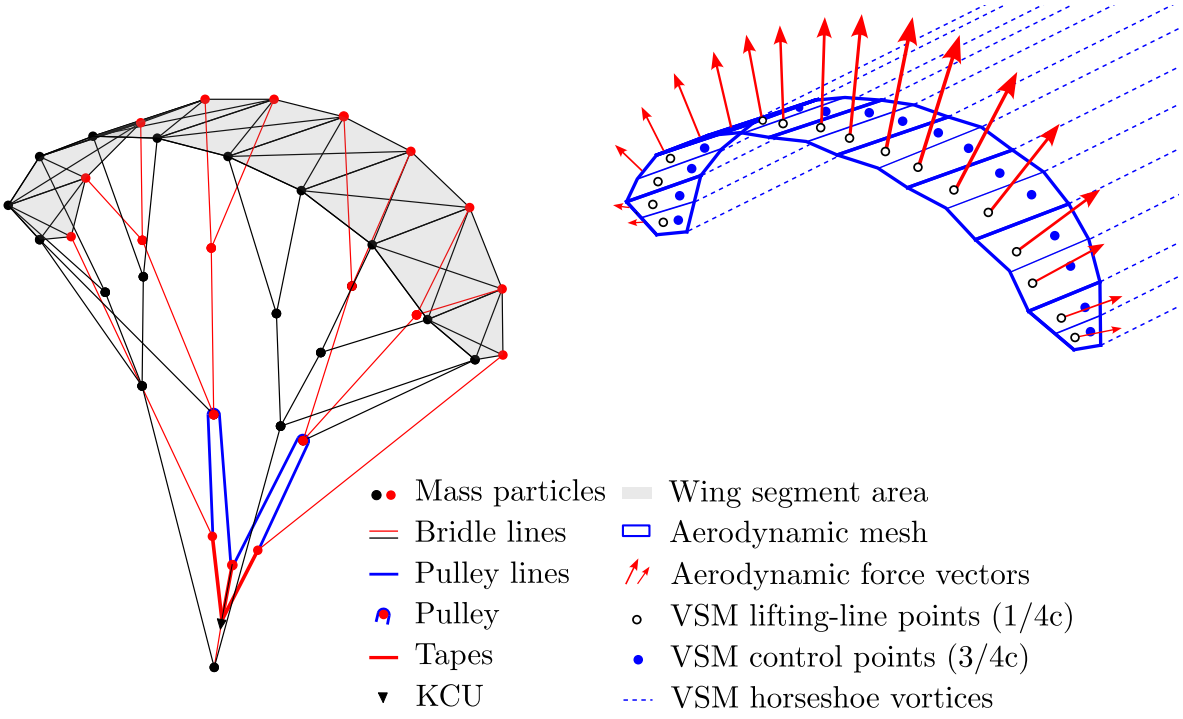

(a) Structural PSM model

(b) Aerodynamic VSM model

Figure 2.2: FSI model of the TU Delft V3 Kite [37]

2.3. Deformations

A LEI kite has little rigidity apart from the inflatable struts. The kite shape is enforced by balancing aerodynamic forces and opposing load through the bridle system [19]. A soft-wing kite typically does not steer using the deflection of aerodynamic surfaces, like in an aeroplane. Instead, steering lines are pulled on to deform the kite such that it enters a turn. In aeroplane terminology, this would be similar to a morphing wing. Controlling the angle of attack, or increasing the lift, is done by pulling on the power lines. The same lines can also be used to stall the kite. Both deformation types are shown in Figure 2.3.

Asymmetric steering inputs used for steering the kite can lead to difficulty in simulation. Models that are resolved in a quasi-steady manner require an equilibrium point for every time step. Finding such an equilibrium point is challenging due to the inherent instability of the kite. While pitch and yaw are stable, roll is not, and the model is only constrained translationally at the bridle attachment point. As a result, asymmetries like those introduced by a steering input can prevent convergence of the model.

The membranes in the kite also deal with wrinkling effects due to deformations in the canopy. Wrinkling is challenging to capture in a model, and wrinkling models are required to resolve this [45].

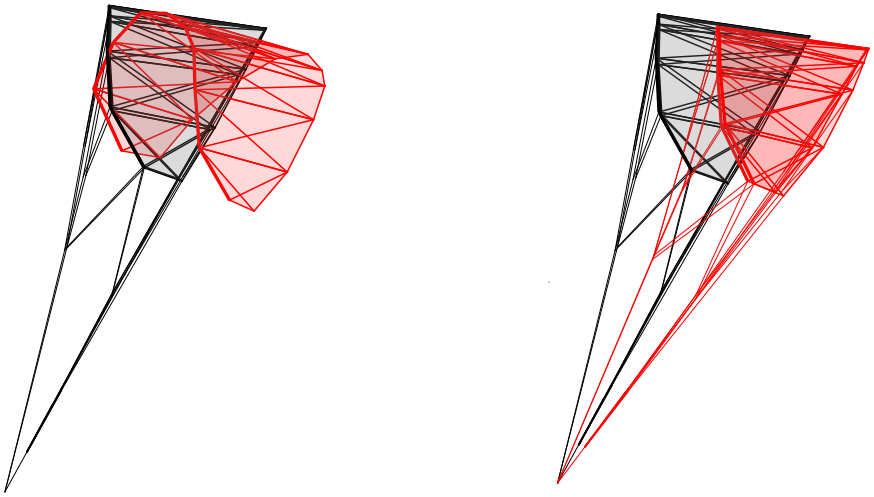

Figure 2.3: Kite deformation due to inputs from the kite control unit [36]. (a) Asymmetric deformation (red) due to a steering input on the kite from the powered state (grey). (b) Depowering of the kite (red) from the powered state (grey)

2.4. Vibrations

Apart from deformations due to inputs on the bridle lines, kites experience other deformations, some of which are oscillatory. These deformations range from global to local phenomena, varying between small and large timescales. A structural model should be able to replicate the most impactful of these modes, as they can significantly affect kite performance or even cause mission failure. The quasi-steady modelling approach can capture the large-scale deformations [27]. Leuthold [27] gives an overview of the various modes shown in Figure 2.4.

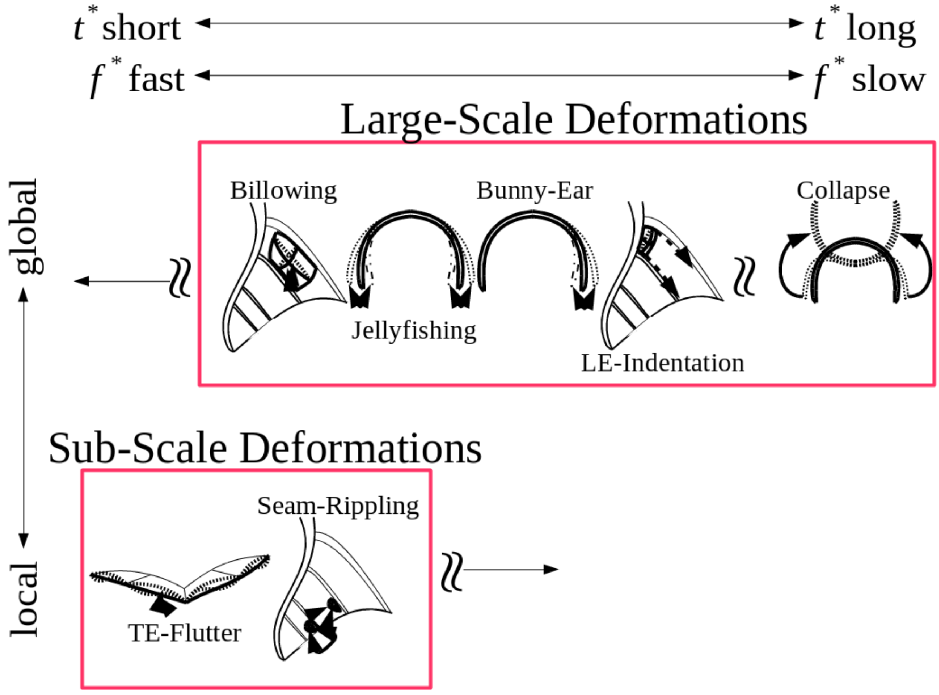

Figure 2.4: Kite deformation modes experienced during a pumping-cycle operation [27]

As explained by Leuthold [27], the modes are as follows.

Large-scale deformation modes

- **Billowing:** The inflation and curvature of the canopy between structural members due to pressure differences. The airfoil shape is affected, and the aerodynamic characteristics are also changed.
- **Jellyfishing:** Spanwise oscillatory bending motions resembling the movement of a jellyfish.
- **Bunny-ear:** During a turning motion of the kite, one tip of the kite starts oscillating in and out.
- **Leading edge indentation:** Localized indentation of the leading edge caused by high loads or insufficient inflation pressure. This indentation is the first stage of collapse, but it can still be recovered.
- **Collapse:** Collapse occurs after extreme leading edge indentation. The shape can no longer be maintained, and the kite inverts. When this occurs, there is a high likelihood of crashing the kite.

Sub-scale deformation modes

- **Trailing edge flutter:** Trailing edge flutter occurs at the trailing edge of the canopy, which starts oscillating due to vortex shedding and causes noise.
- **Seam-rippling:** Seam rippling is a wave that appears near the trailing edge close to the struts.

Large-scale deformations significantly affect power production, either due to failure or significant changes in the aerodynamics of the kite. As such, it is interesting to see if the FSI model can resolve these. For modelling billowing, the structural model must include a canopy model. Jellyfishing and bunny-ear require modelling the bending and torsional stiffnesses of the inflatable beams. Capturing leading-edge indentation and collapse could be more difficult, as the structure undergoes extreme deformations and requires non-linear modelling. The structural model used by Poland [37], shown in Figure 2.2, does not model deformation of the canopy or bending or torsional stiffness of the struts, and the model can therefore be expanded upon.

2.5. Structural models

An overview of previously developed models and their advantages and disadvantages is required to identify a suitable model. An overview of the existing models for modelling deformation and their degrees of freedom (DOF) in a LEI kite is given in Figure 2.5. While only an aspect of computational cost and model runtime, higher DOF models typically require more computation.

2.5.1. Multi-plate

Multi-plate models discretise the kite into several plates hinged at the leading edge. This discretisation into multiple plates crudely models the deformation of the kite and the change in centre of gravity, both neglected in rigid kite models [24]. The plates are connected at the leading edge by rotational springs. The model uses non-physical springs, which need to be tuned to build the model. The first multi-plate model was developed by Landsorp et al. [22, 23]. A three plate model was developed for a flight controller by van Til et al. [47]. Later, the V3 kite was modelled with a varying amount of plates for use in FSI by Poland [19], who reported

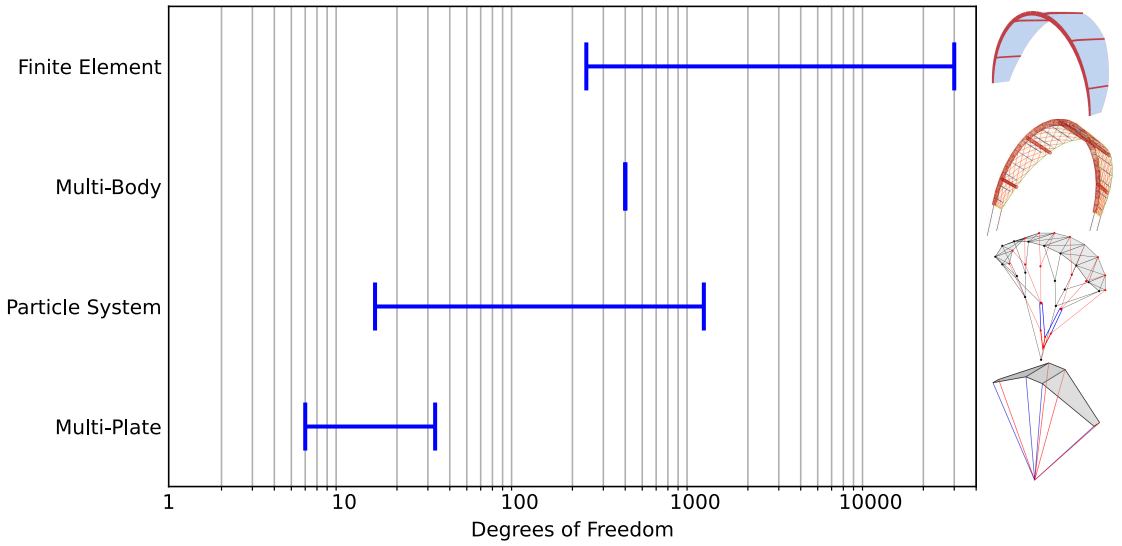

Figure 2.5: Variation in DOF of developed LEI structural model types, model figures from [4, 6, 19]

a 2 ms runtime for a seven plate model. However, Poland found the model incompatible with FSI problems due to its inability to deal with asymmetric actuation inputs.

2.5.2. Lumped mass / particle system

Lumped mass models discretise the kite into multiple particles connected by springs. The first particle-based model for a kite was developed by Furey et al. [14], who modelled a kite with particles and translational springs. The model was coupled to an aerodynamic model to create a flight controller. Later, van der Knaap [21] developed a method to model the bending stiffness of the inflatable tubes by building pyramid elements from particles and linking them with rotational springs. The method was not implemented on the scope of a kite. While the model can resolve bending, the computational time of a rotational spring is about 10 times higher than that of a conventional spring, and by including the required pyramids, the computational cost is 30 times that of a conventional spring [21]. Fechner et al. developed a more reduced approach for control systems of a kite, modelling a kite with four particles. Geschiere adapted the model [15] by developing a particle-based bridle model, which he coupled to the FSI solver of Bosch [4]. Karadayi [20] applied the model by Fechner et al. to a rigid-wing kite. Poland [19] also developed a particle system model of the V3 kite. The entire kite and bridle system is modelled as particles and springs. The PSM was later coupled to an aerodynamics solver [37, 8]. While this resulted in a relatively fast model (10 s for the kite), the model cannot resolve the inflatable beams' bending stiffness. Furthermore, a PSM has difficulty computing high stiffness elements like tethers, requiring small time steps for convergence.

2.5.3. Multi-body

Breukels [6] developed a kite simulation toolbox in MSC Adams and used a multi-body approach to develop a structural kite model. The leading edge tube and the struts consist of rigid elements hinged and connected with torsional springs. The canopy is modelled with linear springs. As noted by Bosch [4], the limitation of this model is the reliance on artificial elements and parameters without a physical meaning that need to be tuned to simulate the physics of the kite.

2.5.4. Finite element

Schwoll [41] developed a detailed finite element model (FEM) in the Madymo software. The beams are modelled as pressurised membranes, and the canopy as a membrane. Physical parameters can be used to describe the membranes. Therefore, the model can capture the physics of the kite correctly. The drawback of Schwoll's model is its complexity, consisting of over 30.000 DOF. Bosch noted this [4], and therefore developed a reduced finite element model in Matlab. The main reduction in complexity comes from describing the LEI tube and the struts as beam elements. Bosch's method ran approximately 25–30 times slower than real time, with an estimated speed-up factor of 5–10 when switching to a compiled language [4]. Computing power has greatly increased since Bosch's model was developed in 2012. A more reduced method to determine the kite's shape was developed by de Solminihac et al. [42], who captures all of the kite properties into beam segments. This is a considerable simplification, and while a rapid approach, non-physical parameters have to be tuned to derive the equivalent beam properties. A ram-air kite has been modelled using membrane elements by Thedens [46], who wrote a finite element solver for membranes in Python [45]. The model was coupled to an aerodynamic solver. Declercq made another finite element model for use in FSI [10]. Declercq modelled the V3 kite in Abaqus. Simplifications were made, as the inflatable tubes were modelled as a solid with non-physical material properties. Furthermore, the canopy was thickened to increase convergence. Declercq reported low confidence in the structural model results due to low deformations [10].

Table 2.1: An overview of structural models for modelling a LEI kite in order of increasing DOFs.

Author	Year	Kite Model	Description	Model DOF*
Lansdorp et al. [22, 23]	2007	Multi-Plate	Two plate model	6
van Til et al. [47]	2018	Multi-Plate	Three plate model for flight control	12
Fechner et al. [11]	2015	Particle System	Four point model for flight control	15
Karadayi [20]	2016	Particle System	Four point model for rigid kites	15
Lansdorp et al. [24]	2008	Multi-Plate	Four plate model for flight control	18
Poland and Schmehl [19, 36]	2022	Multi-Plate	Seven plate model for FSI	33
Furey et al. [14]	2007	Particle System	13 point kite model for flight control	39
Poland [37]	2022	Particle System	37 point model for FSI	111
de Solminihac et.al. [42]	2018	Finite Element	Simplifies entire kite as a spanwise beam	240
Breukels [6]	2011	Multi-Body	Models beams as hinged rigid bodies and the canopy using springs	400
Van der Knaap [21]	2013	Particle System	Derives beam elements using rotational springs. DOF extrapolated to V3 Kite	1122
Bosch [4]	2012	Finite Element	Models the beams as finite elements, and the canopy using shell elements	1332
Schwoll [41]	2012	Finite Element	Models the beams as inflated membranes, and the canopy using membranes	30000
Declerq [10]	2022	Finite Element	Models the kite as a solid, with unphysical material properties	30000

***** Not all models have their DOF stated in the reference and are therefore estimated.

2.6. Geometric non-linear modelling

To elaborate on the non-linearity problem of a kite, an example by Bosch [4] is provided in Figure 2.6. A fully horizontal canopy has no stiffness in the vertical direction, as the material can only be stressed in the direction of the fabric. Calculating the deflection from that situation would lead to a very large or infinite deflection. If geometric non-linearity is considered, then the solution would find a deflection that balances the canopy forces with the aerodynamic forces. The solution has to consider that the direction of the canopy stiffness changes due to the change in geometry.

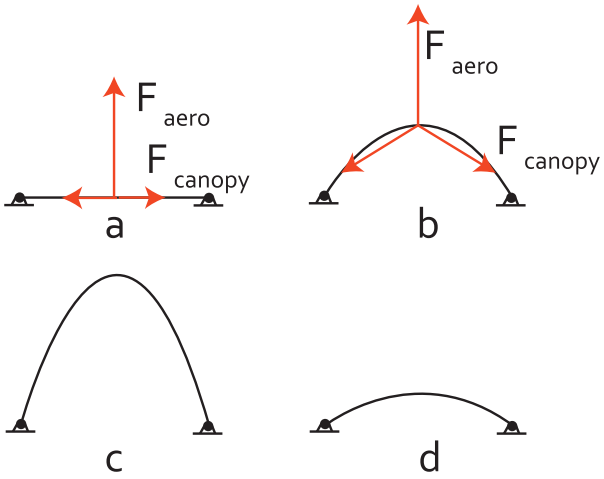

Figure 2.6: Example of geometric non-linear behaviour [4]. (a) Forces in a non-deflected situation. (b) Forces in a deflected situation. (c) Linear deflection. (d) Non-linear deflection

Three frameworks for dealing with geometric non-linearity exist [12].

- **Total Lagrangian framework:** In the total Lagrangian framework, the equations are formulated with respect to a fixed reference configuration, which does not change during the analysis. Often, this reference configuration is described by the initial configuration.
- **Updated Lagrangian framework**: The equations for each new step are related to the solution from the previous step. As the simulation moves forward, this starting point is constantly updated to the latest solved shape.
- **Co-rotational framework:** The element's motion is split into a rigid body motion and a deformational motion. The rigid body motion describes the large-scale translation and rotation of the element in space, while the deformational motion describes the element's change in shape.

The FEM model by Bosch [4] was developed in the total Lagrangian framework, but notes an interest in using the co-rotational framework. The co-rotational framework can effectively treat problems with large rotations but small strains [12]. This makes it an ideal candidate for developing a model of the kite bridle system and tether. The elements in the aforementioned pyfe3d codebase by Castro [7] are described using the co-rotational framework.

2.6.1. Form finding

Form finding is a field that is focused on finding the shape of structures and systems and is defined by Veenendaal and Block [48] as follows: "Finding a shape of equilibrium of forces in a given boundary with respect to a certain stress state". Such methods apply directly to the kite deformation problem, as there is a significant geometric non-linearity in the system. Given a structural problem, the form-finding method is interested in finding the static solution

of Equation (2.1). The static solution then reduces to Equation (2.2). Since the structural model to be developed is quasi-steady, the dynamics do not need to be included, and a static solution is sufficient.

$$\mathbf{M\ddot{u}} + \mathbf{C\dot{u}} + \mathbf{Ku} = \mathbf{f} \tag{2.1}$$

$$\mathbf{Ku} = \mathbf{f} \tag{2.2}$$

Veenendaal and Block have categorised form-finding methods [48] into three categories, as shown in Figure 2.7.

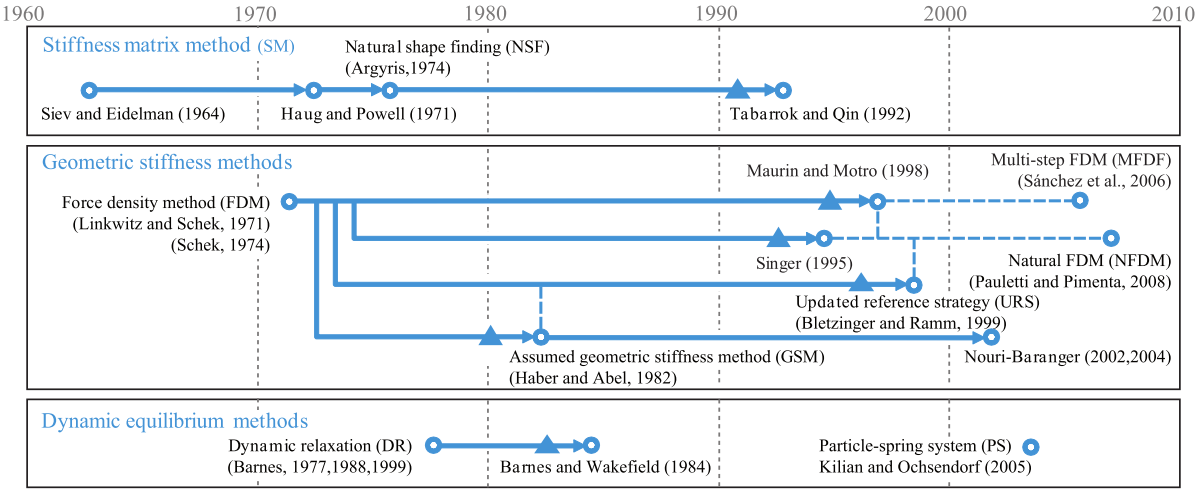

Figure 2.7: Development of various form-finding methods and their respective references, with arrows denoting descendents, dotted lines denoting related but independent methods and triangles denoting a first formulation of surface elements [48]

.

Stiffness matrix method

In the stiffness matrix method, one attempts to solve the problem as a structural problem. The system's elastic and geometric stiffness matrix is set up using one of the non-linear frameworks. Then, the stiffness matrix forms a system with the set forces and boundary conditions. The system is then solved for displacements. Geometric non-linearity is solved using the total Lagrangian formulation, updated Lagrangian formulation or the co-rotational formulation [44]. The system can then converge to a solution using Newton-Raphson iteration. Common criticism of the stiffness matrix method is the inclusion of material properties in the equations, which are not explicitly needed to come to a solution and could lead to difficulty in convergence control [1, 18, 33].

Geometric stiffness method

As the name implies, geometric stiffness methods focus on finding a solution using only the geometric stiffness while disregarding the elastic stiffness. The first method developed was the force density method. Force densities and geometric stiffnesses are not intuitive properties. Therefore, they might be challenging to work with [18, 33]. Furthermore, the linear form of the method is only applicable to preliminary results [1] as the linear results depend on mesh density and anisotropy [48].

Dynamic equilibrium method

Dynamic Equilibrium methods reintroduce a mass and damping matrix, arriving again at Equation (2.1). In this case, the mass and damping matrix can be entirely fictional and tuned for convergence. The intermediate values are non-physical, but the system converges to a static solution. Dynamic equilibrium methods require many parameters for stability and convergence [33]. Including non-physical mass and damping matrices could be viewed as a disadvantage. However, these matrices can be tuned to improve convergence and stability and can therefore also be viewed as advantageous [2].

2.7. Beam Modelling

2.7.1. Inflatable beams

Inflatable beam structures are made out of membranes that can carry little load. The structural strength comes from the pre-stressing of the membrane due to internal pressure [52]. As such, the structural behaviour of inflatable beams is dictated by material, geometry, shape, and loads more so than rigid beams [49]. Inflatable beams can return to their original shape without any elastic deformation. The first part of the stress-strain deflection curve of an inflatable beam is linear, and the beam can be observed to be taut. Once the loading on the beam is such that the pre-stress is counteracted by the loading, wrinkles start to appear and later collapse [9]. Once wrinkling appears, the response is no longer linear. A comparison of a typical stress-strain curve for a conventional beam and an inflatable beam is given in Figure 2.8.

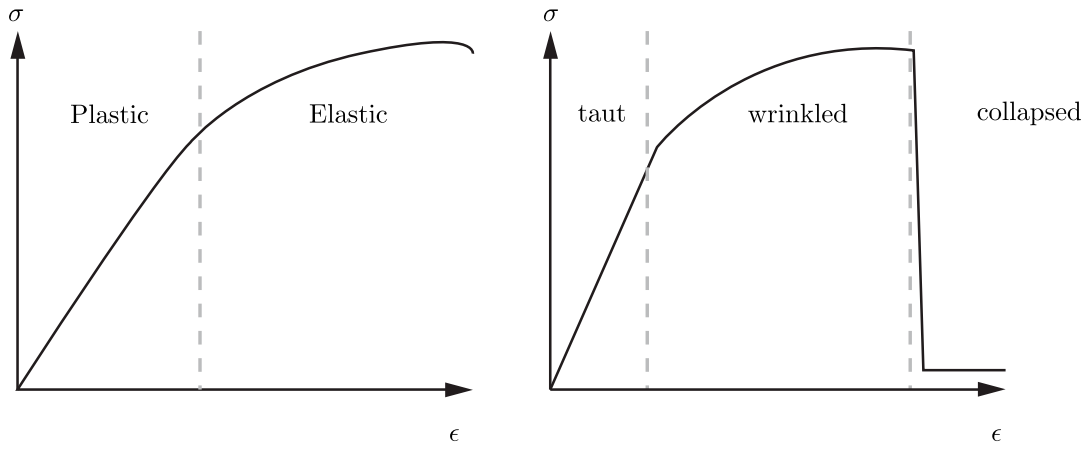

Figure 2.8: Stress-strain curve of a homogenous isotropic beam and an inflated tubular beam [2, 5]

Breukels [6] developed analytical functions for inflatable beam deflection and torsion based on measurements from a test setup. The following relations of a cantilever inflatable beam with a length of $1\ \mathrm{m}$ loaded on the tip are found and approached with analytical functions.

$$T = f(p, r, \varphi) \tag{2.3}$$

$$P = f(p, r, v) \tag{2.4}$$

Notably, the dependency of the tip load on the deflection leads to a non-constant value of EI, which would be constant throughout a conventional beam.

$$EI(p, r, v) = \frac{P(p, r, v)\, L^3}{3v} \tag{2.5}$$

Bosch [4] chose a single value for EI to simplify the beam model. This over-predicts the stiffness when dealing with large deflections, and under-predicts the stiffness when dealing with small deflections.

2.7.2. Beam modelling in FEM

Within FEM, beams can be modelled as conventional Euler-Bernoulli beam elements or Timoshenko beam elements. These elements are typically available in FEM libraries. Therefore, they are simple to implement. Le Van and Wielgosz [25, 26] developed a finite element formulation specifically for modelling inflatable beams. Such an implementation directly makes use of pressure inside the stiffness matrix. Alternatively, one can model an inflatable beam as a membrane with internal pressure [16]. Schwoll's [41] FEM uses this approach. However, such an approach is computationally expensive. Lastly, one can base Timoshenko beam element's stiffness off of Breukel's fitted equations, as performed by Bosch [4].

2.7.3. Beam modelling in PSM

Modelling a beam in a PSM is not an intuitive process, as a linear spring has no bending stiffness. Two approaches are available to model a beam with springs. The first approach is used by van der Knaap [21] as seen in Figure 2.9. Pyramids were formed from particles and connected with stiff springs to form rigid bodies. These were then hinged onto the next pyramid using rotational springs. The rotational springs were tuned such that the beam represents the deflection of a beam.

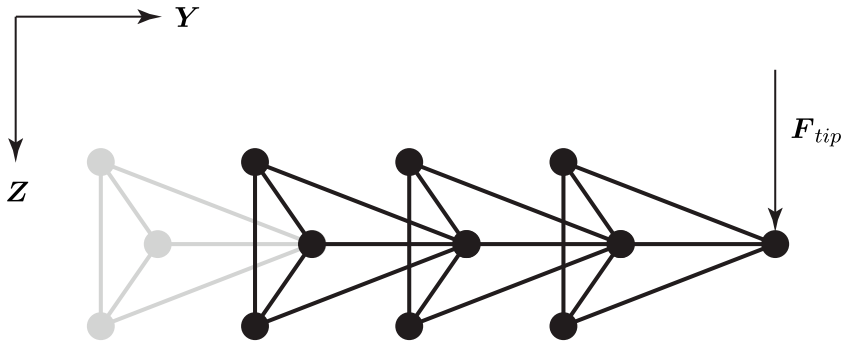

Figure 2.9: Beam representation in a PSM based on rigid pyramids hinged with rotational springs [21].

An alternative approach is to form a truss-like structure from particles and springs. A particle spring assembly can be made and the spring stiffnesses tuned such that the assembly is equivalent to a beam segment [30, 53, 51]. The assembly shown in Figure 2.10 shows an equivalent particle spring assembly consisting of eight particles and 24 springs. The springs were grouped in six stiffnesses, and their values can be determined using energetic equivalence [53]. This means that an equation is set up for all six deformation modes (three axial and three shear). The energy stored in the springs should equal that of the equivalent beam. The energy stored in the beam is derived from the beam properties E and G. The six springs' stiffnesses can then be determined to define the particle system assembly representing a beam segment. A similar approach by Sabzehzar et al. [39] describes an equivalent Timoshenko beam for truss structures, again showing the two systems' equivalence.

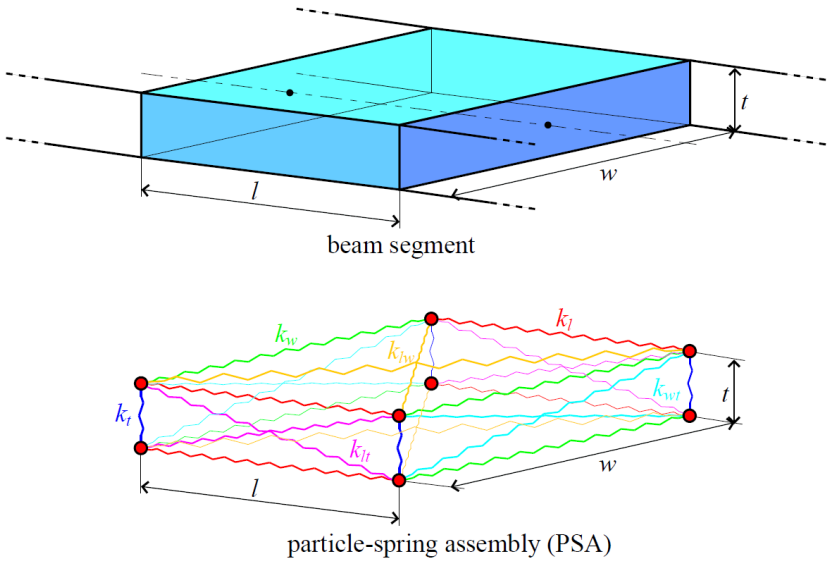

Figure 2.10: Equivalent beam segment and particle spring assembly used to represent a beam in PSM [53, 51]

2.8. Research objective and questions

This literature study analyses the challenges and methods for the structural modelling of LEI kites used in AWE. The challenge in modelling a LEI kite lies in the flexible nature of the kite, leading to a significant coupling between aerodynamic loads and structural deformation. A kite's various deformations and vibrations are discussed, and the large-scale deformations are deemed important to resolve for a good power production estimation. Existing structural models of LEI kites are shared, and their advantages and limitations are discussed. A review of the current models shows a distinct trade-off between computational speed and physical accuracy. With an interest in including bending and torsion of the inflatable beams into the model, two options for new models are selected. A high-fidelity PSM and a low-fidelity FEM are identified as competitive options moving forward, and the methodology of implementing bending stiffness in both is discussed. The remainder of this thesis will focus on the development of an open-source, fast, and sufficiently accurate structural modelling approach for LEI kites.

The research objective of the thesis is set as follows:

What modelling approach enables a computationally efficient structural model for leading-edge inflatable kites that captures the inflatable structure's bending and torsional stiffness?

Accompanying the objective, the following research questions are addressed in the study.

1. Which framework is most suitable for developing a LEI kite structural model?
2. How can the structural model be coupled to the aero-structural framework?
3. To what extent can the developed method resolve large-scale kite deformations?
4. How does the model compare to experimental measurements?

3

Model selection

Both a low-fidelity FEM and a high-fidelity PSM are selected as promising methods to use for modelling bending in LEI kites. Both options will add complexity to the existing PSM model, as described by Poland [19]. The chosen modelling approach needs to be both accurate in representing the bending behaviour of a beam and minimal in terms of complexity. Both approaches are tested on a cantilevered beam case, described in Section 3.1. The setup of both PSM and FEM approaches is shared, the results of the two approaches are compared and a model is selected to develop in Section 3.2.

3.1. Cantilevered beam case

The cantilevered beam is a classic example used in beam theory, the case is visualised in Figure 3.1. A beam, of length L, is clamped at $x = 0$ and has a vertical load P applied at the tip. The beam has cross-sectional properties A and I, corresponding to area and area moment of inertia. Furthermore, the beam material determines the Young's modulus E. For small loadings, often only the deflection w in the y direction is described. along with tip angle θ_0. For larger loadings, a deflection u in the x direction becomes more pronounced, and a geometrically non-linear modelling approach is required to solve this displacement. Normalised vertical deflection w/L, horizontal deflection u/L and rotation θ_0 curves based on a load parameter $\frac{PL^2}{EI}$ were numerically obtained by Mattiason [32].

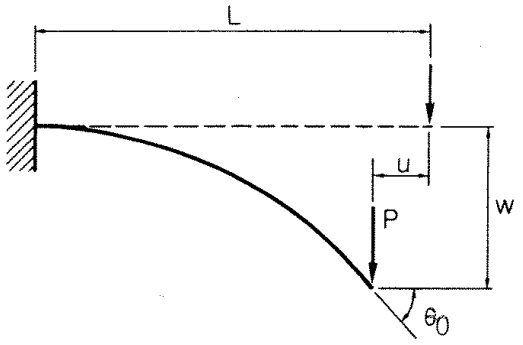

Figure 3.1: The cantilevered beam case with vertical loading on the free end [32]

3.2. PSM and FEM comparison

A finite element model of the beam was set up to represent the cantilevered beam. The beam was modelled using Timoshenko beam elements, the element description was provided by pyfe3d [7] based on the formulation by Luo [29]. The full setup of the non-linear finite element model can be found in Chapter 5.

The particle system framework by Batchelor [2] was used to model equivalent beam sections using springs as shown before in Figure 2.10. For equivalent beam sections with equal side lengths, it was found that the spring stiffness could be tuned to represent the bending stiffness EI of the equivalent beam with $k \approx \frac{EI}{2.4l^3}$. With an increasing amount of discretisation this approach matched closely the results of Mattiason across the entire loading-deflection curve. An example of a beam modelled in this framework is provided in Figure 3.2.

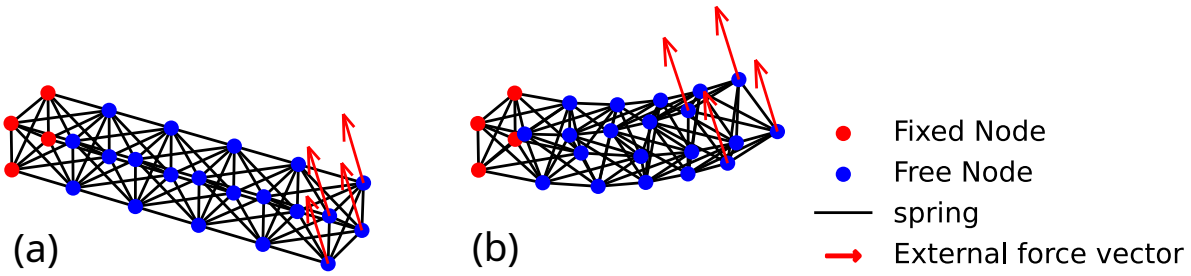

Figure 3.2: (a) The initial cantilevered beam configuration represented with springs in the PSM. (b) The resulting deformation for a load parameter of two, applied at an angle

Both model types were modelled with varying amounts of discretisation. It should be noted that by adding a element to the finite element model, one node with six DOF's is added, of which three are translational and three rotational. Adding a equivalent beam segment to the PSM representation of a beam adds four particles (or nodes), each with three DOF's, all translational, totalling 12 DOF for an extra beam segment. This means that finely discretising a beam in the PSM adds twice the amount of DOF than when using FEM. Furthermore, a PSM equivalent beam segment leads to 24 spring connections, which lead to more non-diagonal entries in the stiffness matrix and therefore a more complex system to solve.

The results of the PSM cantilevered beam, modelled with two and five equivalent beam sections are presented alongside the results of the FEM cantilevered beam, modelled with one and three elements. Both results are compared to the numerical results of Mattiason in Figure 3.3a and b. One can see that a high DOF PSM representation captures the non-linear behaviour very well, at a high computational cost. The lower DOF PSM representation is an okay fit, but still at a high computational cost. In comparison, even a low DOF FEM representation works very well up to load parameters of three, corresponding to rather large deflections. Comparing the two model types in terms of complexity and accuracy, the FEM approach is more favourable to scale to a larger kite model, and is therefore selected for modelling the kite.

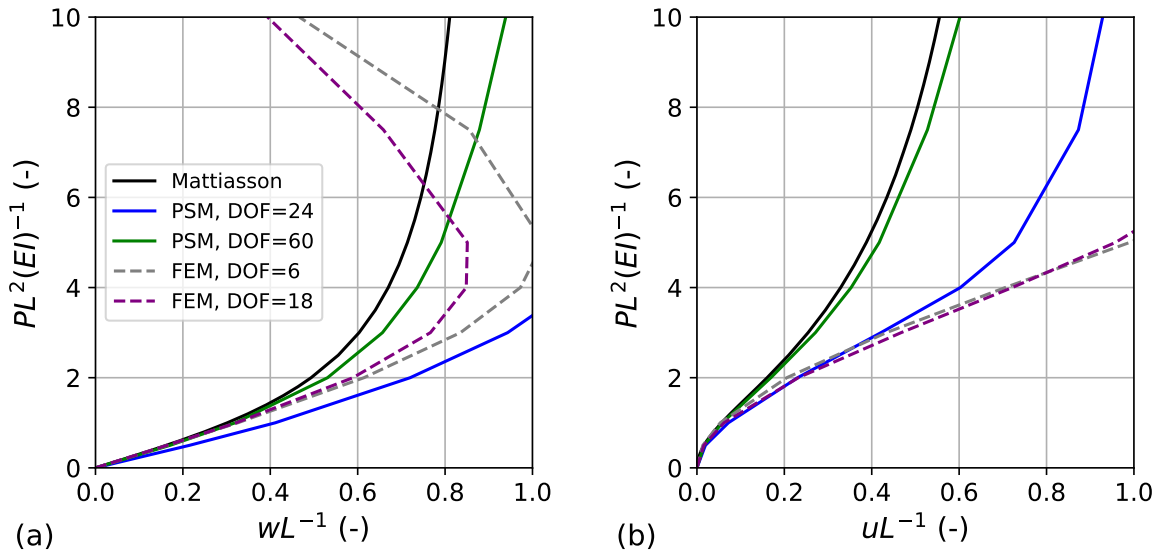

Figure 3.3: (a) Normalised vertical displacement of a cantilevered beam under varying tip loading, comparing PSM and FEM with numerical results. (b) Normalised horizontal displacement of a cantilevered beam under varying tip loading, comparing PSM and FEM with numerical results.

4

Modelling approach

This chapter describes the modelling approach used to couple the aerodynamic and structural behaviour of a leading-edge inflatable kite. A partitioned aero-structural framework is adopted, allowing the structural and aerodynamic models to be developed and evaluated independently while iterating towards a coupled equilibrium solution.

Section 4.1 introduces the overall aero-structural coupling strategy and defines the inputs and outputs of the framework. The structural model, based on a geometrically non-linear finite element formulation, is outlined in Section 4.2, including its integration within the iterative solution loop. Finally, Section 4.3 briefly describes the aerodynamic model used to compute the distributed loads acting on the deformed kite geometry.

4.1. Aero-structural model

The partitioned aero-structural model developed by Poland and Cayon [37, 36, 8] will be adapted to include the newly developed structural model. Figure 4.1 shows how the aero-structural problem is solved iteratively by feeding the output from the structural model into the aerodynamic model, and vice versa, until convergence. The inputs for the model are:

1. **Steering and power input:** The lengths of the steering lines an power lines are set as an input, such that one can vary them and see the corresponding aero-structural response.
2. **Surfplan model:** Surfplan [43] is a CAD software for kites. The model is fed through surfplan adapter [34], which prepares geometrical and aerodynamic inputs to use in the structural and aerodynamic model.
3. **Apparent velocity:** The velocity seen by the kite is used as an input for the aerodynamic model to determine the aerodynamic loading.

As an output, the kite shape and aerodynamic forces are given. However, one can choose to include more details from the structural and aerodynamic models. The partitioned nature of the model allows for switching between different structural and aerodynamic models. The developed structural model can therefore be inserted in place of the previous model by matching its inputs and outputs with those of the previous model.

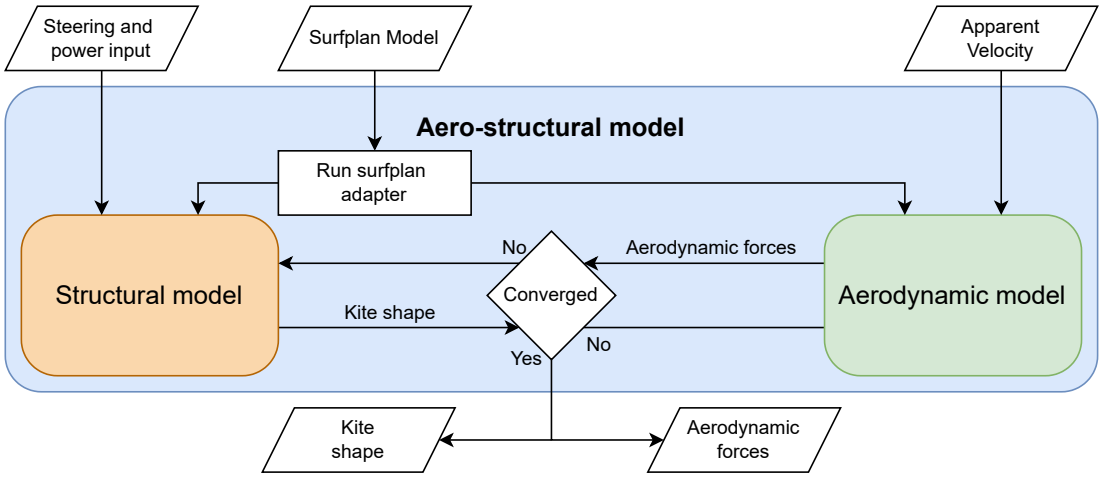

Figure 4.1: Schematic overview of the partitioned aero-structural model

4.2. Structural model

A FEM is developed to fit into the structural model slot in the partitioned aero-structural model. The FEM employs the CRF to address the non-linear geometry. The system is solved using the Newton-Raphson method. An overview of the model is given in Figure 4.2

The model can be set up using the adapted surfplan geometry files, and optionally, the lengths of the steering and power tapes can be adjusted. The model is set up such that all finite elements are defined, all nodal coordinates are defined, and the mass is distributed along the nodes. Then, one can input an aerodynamic loading, which will be used to determine the external forces. Within the Newton-Raphson iteration loop, the displacement iterates towards a position where the internal forces and external forces at each node are balanced. In line with the CRF, the rotational matrix is updated each iteration to track the orientation of individual elements. The stiffness matrix and residual force vector are also set up at each iteration. The displacement is then updated by solving the linear system $\mathbf{K}\Delta\mathbf{u} = \mathbf{r}$. When the normalised residual force vector is below the convergence criteria, the displacement is outputted and added to the initial coordinates to provide the final kite shape.

4.3. Aerodynamic model

The vortex-step method is used as the aerodynamic model. This model, developed by Cayon [8], iteratively determines the circulation distribution and thereby the lift over the kite's segments. The model is already integrated in the aero structural loop and will not be modified. The model fits within the aerodynamic slot in Figure 4.1

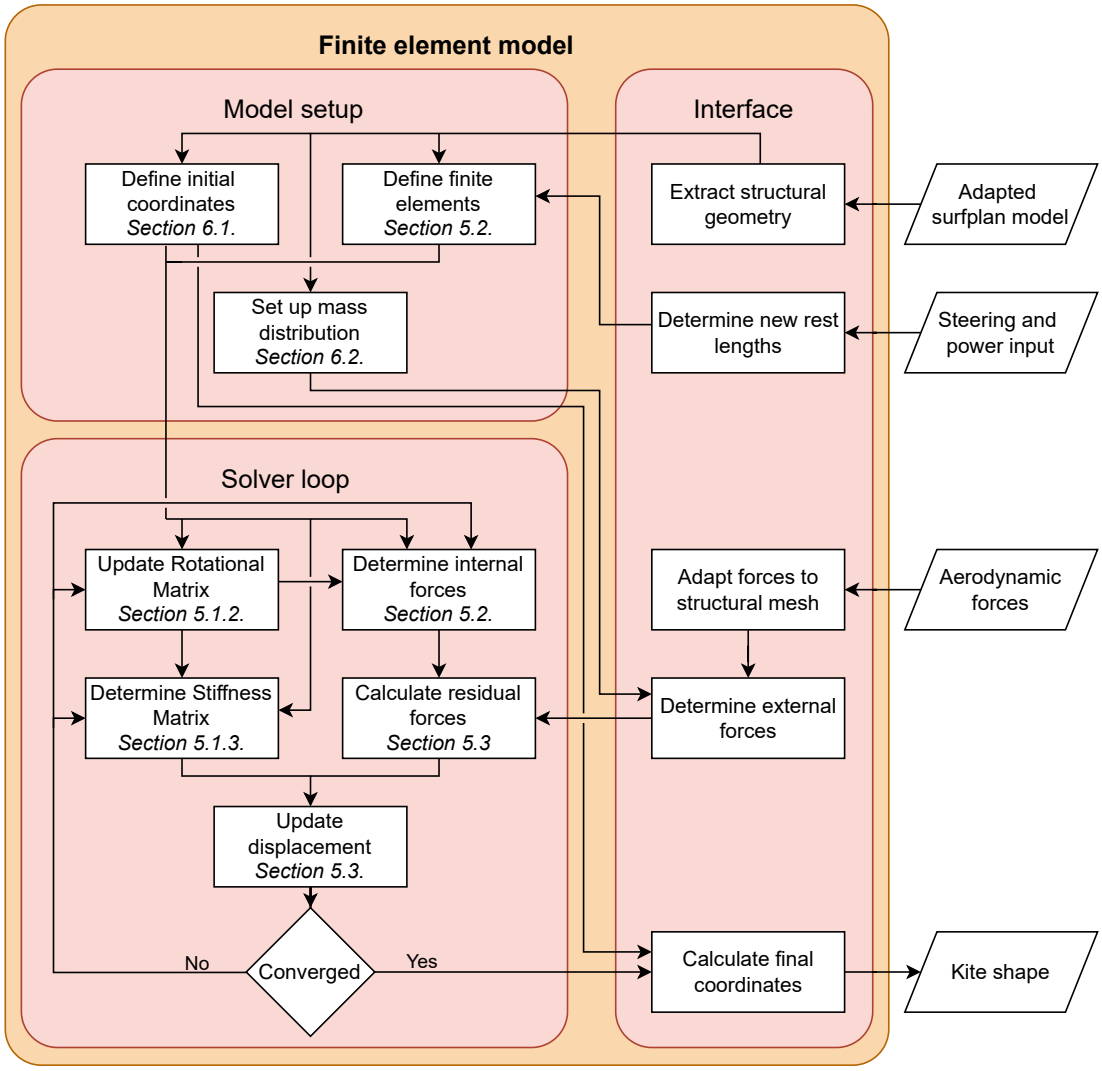

Figure 4.2: Schematic overview of the finite element model

5

Finite element framework for kites

This chapter presents the finite element framework developed to model the structural behaviour of bridled leading-edge inflatable kites. Section 5.1 describes the general finite element formulation and assembly procedure, including the treatment of geometric non-linearity. Kite-specific modelling choices are introduced in Section 5.2, covering the bridle line system, inflatable leading edge and struts, and the canopy. The solution strategy and convergence procedure are discussed in Section 5.3, followed by verification of the framework in Section 5.4.

5.1. Finite element formulation

5.1.1. The two-node finite element

The framework presented in this chapter shows how one can discretise the different parts of a kite into finite elements. The framework makes use of two node elements existing in a a three-dimensional space, the implementation of which is handled through the python package pyfe3d [7]. Figure 5.1 shows an element spanning between nodes n_1 and n_2. Each node has three translational and three rotational degrees of freedom (DOF). In total a two node element has 12 DOF, the displacement vector in the element coordinate system is shown in Equation (5.1). A stiffness matrix, $\mathbf{K}_e$, of dimensions 12×12 is accompanied with each element:

$$\mathbf{u}_e^T = [u_1 \quad v_1 \quad w_1 \quad \varphi_1 \quad \theta_1 \quad \psi_2 \quad u_2 \quad v_2 \quad w_2 \quad \varphi_2 \quad \theta_2 \quad \psi_2]\,. \tag{5.1}$$

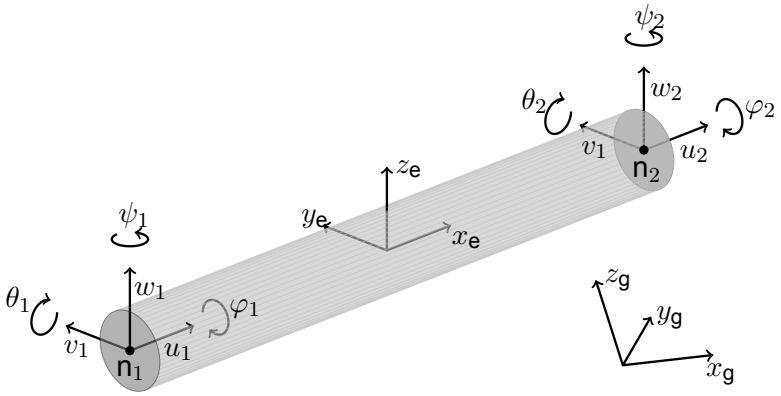

Figure 5.1: A two node element in three-dimensional space with six DOF per node, accompanied by a local coordinate system, adapted from [4].

Each element has a local coordinate system, with the x axis defined in the element's direction $(x_\mathsf{e},\ y_\mathsf{e},\ z_\mathsf{e})$. The element is placed within a global coordinate system $(x_\mathsf{g},\ y_\mathsf{g},\ z_\mathsf{g})$. The element's coordinate frame may be misaligned with the global coordinate frame's orientation. Element deformations therefore need to be mapped onto the global coordinate system.

5.1.2. Coordinate System Transformations

The local coordinate system is defined by constructing a local orthonormal coordinate system using vectors. The x direction is aligned with the element, and a y and z axis is constructed. This allows for quick construction of the rotation matrix, mapping local coordinates to the global coordinate system.

Consider a two-node beam element with global coordinates $\mathbf{x}_1$ and $\mathbf{x}_2$. The element's coordinate system x vector, $\mathbf{x}_\mathsf{e}$, is defined in the direction of the element:

$$\mathbf{x}_\mathsf{e} = \frac{\mathbf{x}_2 - \mathbf{x}_1}{\|\mathbf{x}_2 - \mathbf{x}_1\|} = \begin{bmatrix} x_i \\ x_j \\ x_k \end{bmatrix}. \tag{5.2}$$

Now, the y and z vectors, $\mathbf{y}_\mathsf{e}$ and $\mathbf{z}_\mathsf{e}$ should be constructed. Since all elements used in the remainder of this thesis share the same properties in z and y direction, i.e. the elements are axisymmetric, any orthogonal combination of $\mathbf{x}_\mathsf{e}$, $\mathbf{y}_\mathsf{e}$ and $\mathbf{z}_\mathsf{e}$ is valid as long as $\mathbf{x}_\mathsf{e}$ is aligned with the element direction.

To determine $\mathbf{y}_\mathsf{e}$ and $\mathbf{z}_\mathsf{e}$, a vector $\mathbf{v}_{xy}$ is defined. This can be any vector, with the exception of $\mathbf{v}_{xy} = \mathbf{x}_\mathsf{e}$. The vector $\mathbf{v}_{xy}$ is defined as

$$\mathbf{v}_{xy} = \begin{bmatrix} v_{xyi} \\ v_{xyj} \\ v_{xyk} \end{bmatrix}. \tag{5.3}$$

The element's coordinate system z vector, $\mathbf{z}_\mathsf{e}$, is constructed as the normalized cross product between the element axis and the reference vector:

$$\mathbf{z}_\mathsf{e} = \frac{\mathbf{x}_\mathsf{e} \times \mathbf{v}_{xy}}{\|\mathbf{x}_\mathsf{e} \times \mathbf{v}_{xy}\|} = \begin{bmatrix} z_i \\ z_j \\ z_k \end{bmatrix}. \tag{5.4}$$

And the element's coordinate system y vector, $\mathbf{y}_\mathsf{e}$, is then similarly obtained from

$$\mathbf{y}_\mathsf{e} = \frac{\mathbf{x}_\mathsf{e} \times \mathbf{z}_\mathsf{e}}{\|\mathbf{x}_\mathsf{e} \times \mathbf{z}_\mathsf{e}\|} = \begin{bmatrix} z_i \\ z_j \\ z_k \end{bmatrix}. \tag{5.5}$$

The rotation matrix $\mathbf{R}$, mapping local coordinates to global coordinates is assembled by placing the local basis vectors as columns:

$$\mathbf{R} = \begin{bmatrix} \mathbf{x}_\mathsf{e}, \mathbf{y}_\mathsf{e}, \mathbf{z}_\mathsf{e} \end{bmatrix} = \begin{bmatrix} x_i & y_i & z_i \\ x_j & y_j & z_j \\ x_k & y_k & z_k \end{bmatrix}, \tag{5.6}$$

The displacement vector of a two node element has 12 DOF as defined in Equation (5.1). Therefore, the rotation matrix $\mathbf{R}$ is used to construct the 12×12 element rotation matrix $\mathbf{T}$:

$$\mathbf{T} = \begin{bmatrix} \mathbf{R} & 0 & 0 & 0 \\ 0 & \mathbf{R} & 0 & 0 \\ 0 & 0 & \mathbf{R} & 0 \\ 0 & 0 & 0 & \mathbf{R} \end{bmatrix}. \tag{5.7}$$

The element rotation matrix $\mathbf{T}$ is used to map element displacements, forces and the stiffness matrix to the global coordinate frame, and the inverse $\mathbf{T}^{-1}$ is used to map from the global to element coordinate frame. The element contribution to the global coordinate system can then be written as

$$\mathbf{u}_\mathsf{g} = \mathbf{T}\mathbf{u}_\mathsf{e}, \tag{5.8}$$

and

$$\mathbf{f}_\mathsf{g} = \mathbf{T}\mathbf{f}_\mathsf{e}. \tag{5.9}$$

The linear displacement of an element due to a force vector $\mathbf{f}^\mathsf{e}$ in the element coordinate system can be obtained by solving the system

$$\mathbf{K}_\mathsf{e}\mathbf{u}_\mathsf{e} = \mathbf{f}_\mathsf{e}. \tag{5.10}$$

Applying Equations (5.8) and (5.9) to (5.10) leads to

$$\mathbf{K}_\mathsf{g}\mathbf{u}_\mathsf{g} = \mathbf{f}_\mathsf{g}. \tag{5.11}$$

Where the element contribution to the global stiffness matrix is given by

$$\mathbf{K}_\mathsf{g} = \mathbf{T}^\mathsf{T}\,\mathbf{K}_\mathsf{e}\,\mathbf{T}. \tag{5.12}$$

5.1.3. Assembling global stiffness matrix

In a system consisting of more elements, a stiffness matrix needs to be assembled from the individual elements' contribution. Therefore, the individual contribution of the element between n_1 and n_2 is now denoted as

$$\mathbf{K} = \begin{bmatrix} \mathbf{K}_{11} & \mathbf{K}_{12} \\ \mathbf{K}_{21} & \mathbf{K}_{22} \end{bmatrix}, \tag{5.13}$$

where the matrix is split up into four sub-matrices, each with a dimension of 6×6. Similarly, an element between n_1 and n_3 takes the form of

$$\mathbf{K} = \begin{bmatrix} \mathbf{K}_{11} & \mathbf{K}_{13} \\ \mathbf{K}_{31} & \mathbf{K}_{33} \end{bmatrix}, \tag{5.14}$$

where each sub-matrix has a dimension of 6×6. For a system of n nodes $\{n_1, n_2, ..., n_n\}$ the assembled global stiffness matrix has the form of

$$\mathbf{K} = \begin{bmatrix} \mathbf{K}_{11} & \mathbf{K}_{12} & \mathbf{K}_{13} & \cdots & \mathbf{K}_{1n} \\ \mathbf{K}_{21} & \mathbf{K}_{22} & \mathbf{K}_{23} & \cdots & \mathbf{K}_{2n} \\ \mathbf{K}_{31} & \mathbf{K}_{32} & \mathbf{K}_{33} & \cdots & \mathbf{K}_{3n} \\ \vdots & \vdots & \vdots & \ddots & \vdots \\ \mathbf{K}_{n1} & \mathbf{K}_{n2} & \mathbf{K}_{n3} & \cdots & \mathbf{K}_{nn} \end{bmatrix} + c\mathbf{I}. \tag{5.15}$$

Again, the sub-matrices are of dimensions 6×6. The total global stiffness matrix is assembled by adding all elements' contribution to the system. The element between n_1 and n_2 adds contributions to $\mathbf{K}_{11}$, $\mathbf{K}_{12}$, $\mathbf{K}_{21}$ and $\mathbf{K}_{22}$ of Equation (5.15). Similarly, the element between n_1 and n_3 contributes to $\mathbf{K}_{11}$, $\mathbf{K}_{13}$, $\mathbf{K}_{31}$ and $\mathbf{K}_{33}$. Additionally, to deal with geometric non-linearity, a stiffness value is added to each DOF of the stiffness matrix using the identity matrix $\mathbf{I}$. This ensures that a displacement can be calculated in case force is applied on a DOF without any stiffness. The constant c can be tuned for convergence. The assembled global system is then described by

$$\mathbf{K}\mathbf{u} = \mathbf{f}. \tag{5.16}$$

With the method described in this section, one can derive the assembled stiffness matrix of any system consisting of n nodes in three-dimensional space, with a arbitrary amount of two node elements. The global system can be solved for displacements based on a force vector $\mathbf{f}$. A DOF can be fixed by setting the corresponding displacement to zero and removing the corresponding column and row from the matrices and vectors before solving Equation (5.16).

One can see that the rotation matrix is a function of the displacement of the nodes, and therefore the assembled stiffness matrix is as well, i.e. $\mathbf{R}(\mathbf{u})$ and $\mathbf{K}(\mathbf{u})$.

5.2. Kite-specific elements

5.2.1. Bridle line system

The kite is attached to the tether through the bridle line system. The bridle line system enforces the shape of the kite, which is needed to provide lift. The aerodynamic load is transferred through the bridle line system to the tether, which transfers the load to the ground. For AWE applications, bridle line systems are often complex with multiple connection points on the kite, pulleys, and knots in the lines. Furthermore, the steering lines are shortened or lengthened to deform the kite for steering, and the power line is used to increase the angle of attack of the kite. Appendix A shows the full bridle line system of the V3 kite. The bridle lines exhibit relatively small deformations but significant rotations. Therefore, they are ideal to model with FEM using the CRF.

the bridle lines and pulleys are modelled as spring elements. A spring element can only transfer force along its elongation axis, which aligns with the local x axis. Therefore, its stiffness matrix is simple and consists solely of a spring stiffness k_x:

$$\mathbf{K} = \begin{bmatrix} \mathbf{K}_{11} & \mathbf{K}_{12} \\ \mathbf{K}_{21} & \mathbf{K}_{22} \end{bmatrix}, \tag{5.17}$$

$$\mathbf{K}_{11} = \mathbf{K}_{22} = -\mathbf{K}_{21} = -\mathbf{K}_{12} = \begin{bmatrix} k_x & 0 & 0 & 0 & 0 & 0 \\ 0 & 0 & 0 & 0 & 0 & 0 \\ 0 & 0 & 0 & 0 & 0 & 0 \\ 0 & 0 & 0 & 0 & 0 & 0 \\ 0 & 0 & 0 & 0 & 0 & 0 \\ 0 & 0 & 0 & 0 & 0 & 0 \end{bmatrix}. \tag{5.18}$$

For a non-compressive spring, the spring stiffness is set to 0 and back to k_x again based on the current length of the spring,

$$k_x = \begin{cases} k_x & \text{if } (L - L_0) \geq 0, \\ 0 & \text{if } (L - L_0) < 0 \end{cases}. \tag{5.19}$$

The bridle lines can be slack and are therefore modelled as non-compressive springs. Each endpoint of a spring is then a knot, and can be used to attach more lines. Therefore, a bridle line system essentially becomes a combination of non-compressive springs, where each connection point has three degrees of freedom.

The bridle lines are generally made from high-performance materials such as Dyneema, which leads to stiff bridle lines. The spring stiffness used in the model is not representative of the Dyneema material. Using the material properties leads to a stiff system that is difficult to solve. This increases computational costs and affects stability. Therefore, lower stiffnesses are used and tuned so that the final elongation is less than 1%.

A connection of two nodes is shown in Figure 5.2a. This spring spans between n_1 and n_2. The spring has a length of L_{12} and a corresponding rest length L_0.

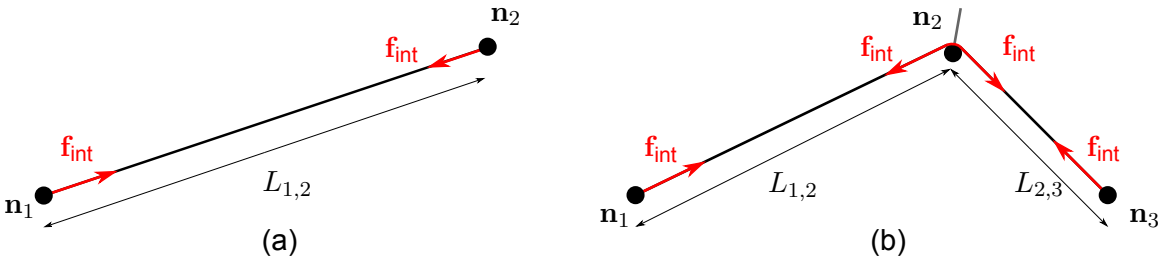

Figure 5.2: (a) Internal forces of a line between n_1 and n_2. (b) Internal forces of a pulley between n_1, n_2 and n_3, where n_2 is the pulley node

The internal force in the element coordinate frame is then calculated by

$$\mathbf{f}_{e,int}^{T} = [k_x(L - L_0) \quad 0 \quad 0 \quad 0 \quad 0 \quad 0 \quad -k_x(L - L_0) \quad 0 \quad 0 \quad 0 \quad 0 \quad 0]. \tag{5.20}$$

Where the value k_x is again adapted to represent a non-compressive spring. The internal force of the element is then transformed to the global coordinate frame and applied to each node using

$$\mathbf{f}_{g,int} = \mathbf{T}\mathbf{f}_{e,int}. \tag{5.21}$$

An ideal, frictionless pulley is modelled as a combination of spring elements. Figure 5.2(b) shows a pulley between nodes n_1, n_2 and n_3. The pulley consists of two spring elements, one between n_1 and n_2, and one between n_2 and n_3. Node n_2 is the pulley node and is free to move across the line. In order to link the two elements into a pulley, the internal force calculation is unified. The total length of the two elements, $L_{123} = L_{12} + L_{23}$ is used in Equation (5.19) and Equation (5.20). The two elements also share the same k_{x} and L_0. This leads to the same magnitude of $\mathbf{f}_{\mathsf{int}}$ across the two elements. By linking these properties node n_2 can move such that L_{12} is shortened and L_{23} lengthened, and vice versa.

For a network of nodes $\{\mathsf{n}_1, \mathsf{n}_1, ..., \mathsf{n}_n\}$, spring connections and pulley connections the internal forces at each node can be determined based on the position of the nodes. Therefore, the internal force vector is a function of the deflection of the system, i.e. $\mathbf{f}_{\mathsf{int}}(\mathbf{u})$.

5.2.2. Leading edge and struts

The leading edge tube and struts of a kite are inflatable structures that provide bending and torsional stiffness due to an overpressure inside the tube. They are used to enforce the aerodynamic shape of the kite and therefore play a vital role. Furthermore, the leading edge tube also acts as a circular leading edge, defining the aerodynamics over the chord. The inflatable structures can be modelled as beam elements, which are two-node elements with 12 DOF, three translational and three rotational per node. The advantage of using beam elements is that the complexity is significantly reduced compared to the alternative option, which involves modelling the inflatable structures as membranes with internal pressure. A beam element relies on material properties and surface cross-section properties to determine the stiffness matrix. The stiffness matrix formulation for a Timoshenko beam element by Luo [29] is used, who describes the explicit expression of the full 12×12 stiffness matrix. The stiffness matrix is a function of beam properties and cross-section properties, i.e. $\mathbf{K}_{\mathsf{e}}(E, G, A, I_y, I_z, k, L)$. For a circular beam the following holds:

$$A = \pi r^2, \tag{5.22}$$

$$I = I_z = I_y \frac{\pi r^4}{4}, \tag{5.23}$$

and $k = \frac{8}{9}$. Thus, all cross-sectional properties rely on r, and k is a constant. The stiffness matrix is then a function of only four variables, i.e. $\mathbf{K}_{\mathsf{e}}(E, G, r, L)$.

Material properties E and G are not directly obtainable for inflatable beams, as the stiffness is dependent on the pressure. Instead, fitted equations by Breukels [6] are used to match the properties of inflatable beams to typical material properties, E and G. Breukels performed bending and torsion experiments on inflatable cantilevered beams of $L = 1$ m, the setup of which can be seen in Figure 5.3.

Breukels derived the following fitted equation to relate deflection with tip force, and rotation with torque:

$$P(p, r, v) = ((C_1 r + C_2)p^2 + (C_3 r^3 + C_4)) \left(1 - e^{-\frac{(C_5 r^5 + C_6)p + (C_7 r + C_8)}{C_1 r + C_2)p^2 + (C_3 r^3 + C_4)} v}\right), \tag{5.24}$$

$$T(p, r, \varphi) = ((C_{13} r + C_{14})p + (C_{15} r + C_{16})) \tan^{-1}((C_{17} r^4 \mathsf{ln}(p) + (C_{18} r^3 + C_{19})\varphi). \tag{5.25}$$

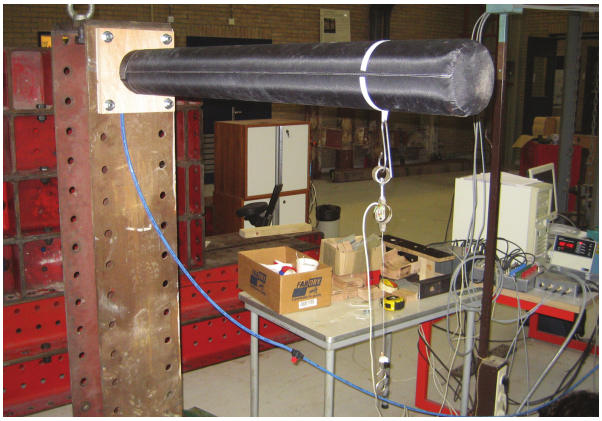

Figure 5.3: Bending test on a one meter inflatable beam [6]

For both equations, the constants are defined in Table 5.1.

Table 5.1: Inflatable beam bending, collapse and torsional constants [6].

Component	Coefficient	Value	Coefficient	Value	Coefficient	Value
Bending	C_1	6582.82	C_4	14.31	C_7	14021.79
	C_2	-272.43	C_5	271865251.42	C_8	-589.05
	C_3	40852.38	C_6	215.93		
Collapse	C_9	322.55	C_{11}	5.3833	C_{12}	0.0461
	C_{10}	0.0239				
Torsion	C_{13}	1467	C_{16}	47.406	C_{18}	358.05
	C_{14}	40.908	C_{17}	-17703	C_{19}	918
	C_{15}	-191.8				

from Timoshenko beam theory the following relations link rotation and deflection with beam properties E and G:

$$v = \frac{PL^3}{3EI} + \frac{PL}{kGA}, \tag{5.26}$$

$$\varphi = \frac{TL}{GJ} = \frac{TL}{2GI}. \tag{5.27}$$

Therefore, E and G can be expressed as:

$$E = \frac{PL^3}{3I(v - \frac{PL}{kAG})}, \tag{5.28}$$

$$G = \frac{TL}{2\varphi I}. \tag{5.29}$$

Breukels' equations for a beam of $L = 1\ \mathrm{m}$ from Equation (5.24) and (5.25) can then be inserted leading to the relations

$$E(p, r, v, \varphi, k) = \frac{P(p, r, v)}{3I(v - \frac{P(p,r,v)}{kAG})}, \tag{5.30}$$

$$G(p, r, \varphi) = \frac{T(p, r, \varphi)}{2\varphi I}. \tag{5.31}$$

The element stiffness matrix can now be defined as a function of p, v, and φ, instead of E and G, i.e. $\mathbf{K}_\mathsf{e}(p, r, L, v, \varphi)$.

The stiffness of the element is not linear and varies with deflection and rotation, and should be updated at each iteration. Therefore, the deflection and rotation must also be updated at each iteration as the element displacement vector $\mathbf{u}_\mathsf{e}$, given in Equation (5.1), changes. Deflection and rotation are then calculated using

$$v = S_v \left\| \begin{bmatrix} u_2 \\ v_2 \end{bmatrix} - \begin{bmatrix} u_1 \\ v_1 \end{bmatrix} \right\|, \tag{5.32}$$

and

$$\varphi = S_\varphi \left| \varphi_2 - \varphi_1 \right|. \tag{5.33}$$

Here, S_v and S_φ are scaling factors to scale the deflection and rotation of an element with length L to that of an element of $L = 1\ \mathrm{m}$, as that is the input required for Breukels' equations. Deflection in a Timoshenko beam scales both with L and L^3, as can be seen in Equation (5.26). The linear part is associated with shear deformation, and the cubic part is associated with bending deformation. To scale element deflections, it is assumed that shear deformation is dominant. This assumption will hold for short elements but will no longer be valid for longer elements. The limits have been investigated and are shared in Subsection 5.4.3. For scaling of rotations, a linear relation is also used, which is directly derived from Equation (5.27). The constants are defined as

$$S_v \approx \frac{1}{L}, \tag{5.34}$$

and

$$S_\varphi = \frac{1}{L}. \tag{5.35}$$

Now, the element stiffness matrix can be set up using pressure, radius, element length, and nodal displacements, i.e. $\mathbf{K}_\mathsf{e}(p, r, L, \mathbf{u}_\mathsf{e})$.

which can be transferred to the global stiffness matrix as described in Section 5.1. The internal forces of a beam element are derived using the element stiffness matrix and element displacement, given by

$$\mathbf{f}_{\mathsf{e,int}} = \mathbf{K}_\mathsf{e}\mathbf{u}_\mathsf{e}. \tag{5.36}$$

5.2.3. Canopy

The goal of modelling the canopy is to capture the global deformation caused by translations, rotations, and element deformation. Part of the canopy of the kite can be modelled by combining four nodes with six non-compressive springs. The membrane material properties are not directly modelled, but are assumed to be very stiff, as the main contribution to the global deformation is due to element translation and rotation. Each non-compressive spring is therefore modelled with high stiffness, such that the elongation falls within one percent of its original length. Figure 5.4a shows how four nodes and six non-compressive springs are combined to represent part of the canopy. Figure 5.4b shows how this integrates further into a kite section, where three sides of the canopy are connected to inflatable beams. The inflatable beam lengths may vary. Therefore, the four-node canopy sections are not square, but quadrilateral. Each node that is not connected to an inflatable beam has no rotational stiffness, and therefore, the canopy sections can hinge around these points.

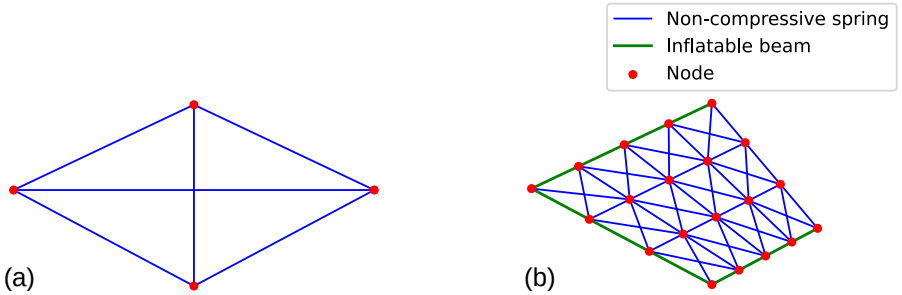

Figure 5.4: (a) Quadrilateral representation of part of a canopy. (b) Example of canopy discretisation within a kite segment

5.3. Newton-Raphson iteration

To get the linear response to a force vector $\mathbf{f}_{\text{ext}}$, only the initial coordinates and element definitions are required and the displacements can be derived from that. The kite has geometric and material non-linearities, which can not be derived linearly. An iterative approach is required to convergence to the solution. Each iteration, the geometry, the material properties and internal forces are all adapted to the displacement $\mathbf{u}$. The Newton-Raphson iteration scheme, presented in Algorithm 1 is used to converge to the solution. Each iteration, all elements' rotational matrices are updated according to the method provided in Section 5.1, using the initial displacement vector, which can be set to zero. The internal forces are calculated with respect to that displacement, as explained in Section 5.2. Then using the external force vector, the residual vector can be determined. The stiffness matrix is also recalculated each iteration based on the current displacement guess. The linear displacement solution is then added to the guess, and the loop restarts until the residual value is converged.

Algorithm 1 Newton–Raphson iteration for geometrically non-linear FEM

Input: Initial guess displacement $\mathbf{u}^0$, tolerance ε, maximum iterations i_{max}, external force vector $\mathbf{f}_{\text{ext}}$, element definitions
Output: Nodal displacement $\mathbf{u}$

$i = 0$
while $i < i_{\text{max}}$ **do**
  Update each elements' rotational matrix $\mathbf{R}(\mathbf{u}^i)$
  Assemble internal force vector $\mathbf{f}_{\text{int}}(\mathbf{u}^i)$
  Assemble residual vector $\mathbf{r}(\mathbf{u}^i) = \mathbf{f}_{\text{ext}} - \mathbf{f}_{\text{int}}(\mathbf{u}^i)$
  Assemble stiffness matrix $\mathbf{K}(\mathbf{u}^i)$ ▷ Elements updated using CRF
  Solve linear system: $\mathbf{K}(\mathbf{u}^i)\Delta\mathbf{u}^i = \mathbf{r}(\mathbf{u}^i)$ ▷ Stiffness matrix acts as Jacobian
  Update solution: $\mathbf{u}^{i+1} \leftarrow \mathbf{u}^i + \Delta\mathbf{u}^i$ ▷ $\Delta\mathbf{u}^i$ can be limited to help convergence
  if $\|\mathbf{r}\| < \varepsilon$ **then**
    return $\mathbf{u}$
  end if
  Update iteration: $i \leftarrow i + 1$
end while

5.4. Verification

5.4.1. Saddle problem

The saddle problem is a form finding problem, where a pre-tensioned spring system is solved to find the equilibrium state. The solution has the form of a mathematical saddle. A square grid is initialized and the border nodes are moved up and down in the z direction, and their DOF's fixed, forming the initial configuration seen in Figure 5.5a. The system is then solved using the scheme explained in Section 5.3. The result for $\|\mathbf{r}\| < 1e^{-3}$ N can be seen in Figure 5.5b.

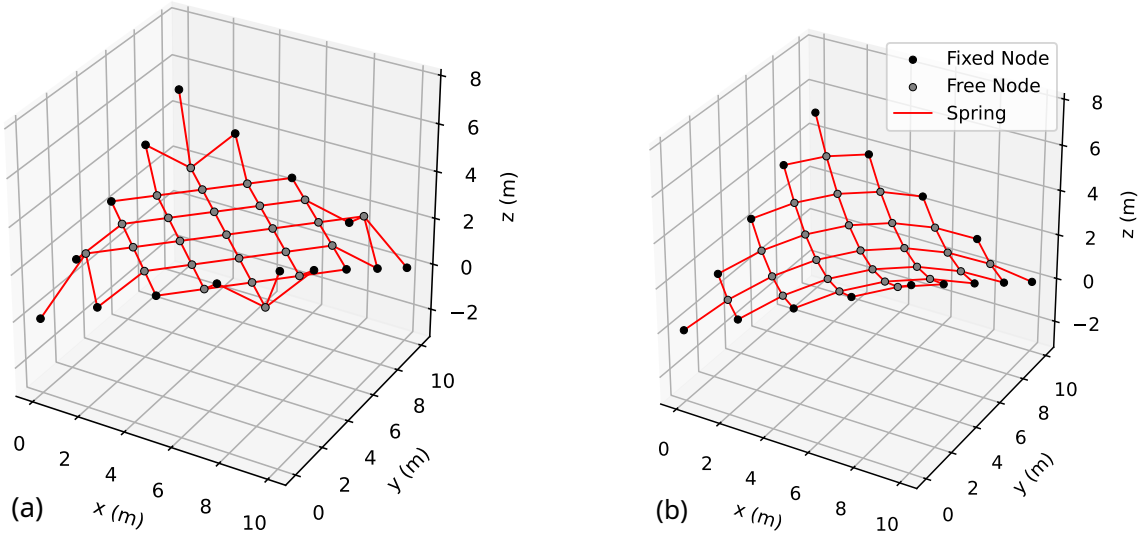

Figure 5.5: (a) Initial conditions of a 5×5 saddle form problem (b) Solution of 5×5 saddle form problem.

The saddle problem is also solved using the PSM with the same convergence criteria. The results of varying grid sizes are compared in Table 5.2. For each node, the difference between the converted PSM and FEM solutions were calculated and the maximum is given in the third column. It shows that both models converge to the same solution. Examining the last two

columns, the FEM solves the system more efficiently than the PSM. As the grid size increases, the computational time of the PSM increases more rapidly than that of the FEM solver. Though it must be noted that the comparison between both methods in terms of speed is not fair, as the finite elements from pyfe3d are modelled in cython, which is a compiled version of python.

Table 5.2: Comparison between FEM and PSM for various saddle problem sizes.

Grid size	Number of nodes	Maximum nodal distance (mm)	FEM solver time (s)*	PSM solver time (s)*
3×3	13	0.06	0.03	0.08
5×5	41	0.10	0.11	0.41
7×7	85	0.16	0.27	1.68
9×9	145	0.27	0.71	2.92
11×11	221	0.38	1.61	5.95
13×13	313	0.49	3.09	18.10

*Using a HP Zbook Power G7 mobile workstation

5.4.2. Nested pulleys

Three pulleys are modelled to verify that the pulley physics are resolved correctly. Four fixed nodes are placed one meter apart. Then, the combinations (n_1,n_5,n_2) and (n_3,n_6,n_4) are set up as pulleys. Furthermore, a pulley system is nested below this with nodes (n_5,n_7,n_6). All three pulley systems have a rest length of 2.2 m A force at a 15° angle from the y axis is applied at n_7. The resulting initial configuration can be seen in Figure 5.6a. The system is solved using the scheme from Section 5.3, and the result is seen in Figure 5.6b. For an ideal, frictionless pulley the angle between the force applied at a node and the two pulley lines should be equal [36]. The angles of the converged state were determined, and it can be seen that $\alpha_1 = \alpha_2$, $\beta_1 = \beta_2$ and $\gamma_1 = \gamma_2$.

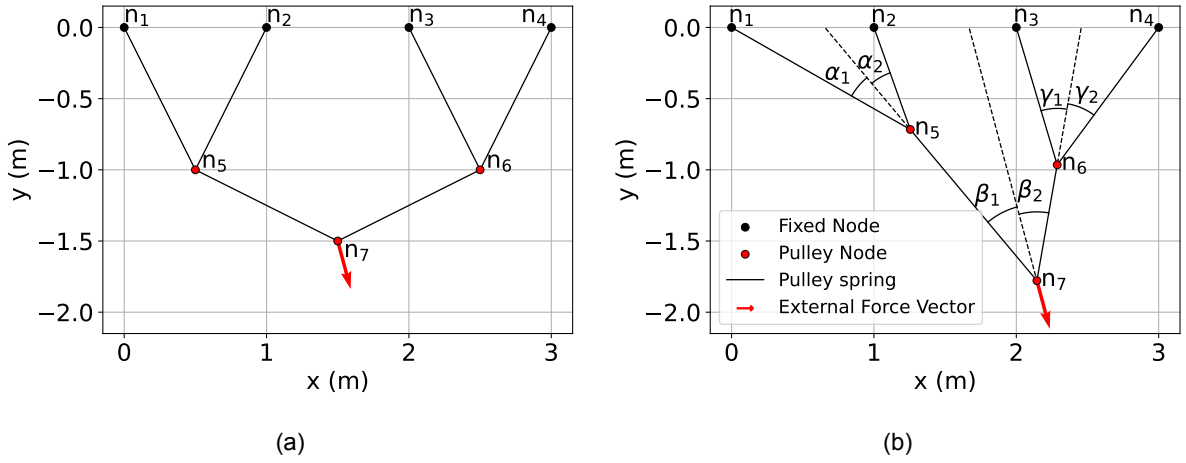

(a) (b)

Figure 5.6: (a) Initial conditions of a nested pulley system (b) Converged solution of the nested pulley system.

5.4.3. Inflatable beam

The approach of modelling inflatable beams as Timoshenko beams, tuned to match inflatable beam properties, was validated against Breukel's fitted equations [6]. A one meter cantilevered beam element under bending and torsion was modelled, and the resulting tip load - deflection and tip moment - deflection angle curves were compared to Equations (5.24) and (5.25). Figure 5.7a shows that the results from the finite element model closely resemble the non-linear

bending and torsional behaviour described by the fitted equations. Torsion is captured exactly, and in bending the finite elements are slightly stiffer. This shows that a one meter Timoshenko beam can be tuned to match inflatable beam characteristics.

To investigate the effectiveness of the scaling approach for elements with a different length than one meter, additional simulations were performed. A range of element lengths was investigated by discretising beams of varying total length, defined as integer multiples of one meter, into one or more finite elements. As a reference solution, beams consisting of validated one-meter elements were used. Both cases are loaded until collapse loading, and the error in deflection compared to the reference case was determined. The results, shown in Fig 5.7b, show that the deflection error remains within a 5% margin between 0.5 and 2 meters. However, for smaller elements, a likely cause of error is that curvature of the beam is captured compared to the reference case and therefore the error is larger. Thus, the inflatable beam element is considered to be valid between zero and two meters.

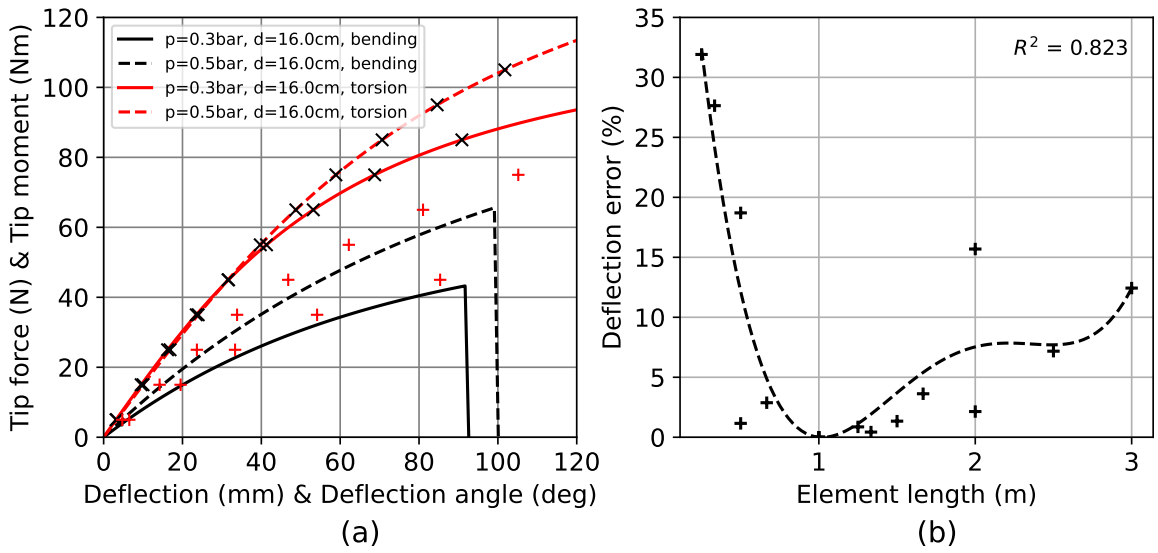

Figure 5.7: (a) Comparison of a one meter beam element to Breukels' fitted equations [6] for inflatable beams, scatter points indicate finite element results and lines indicate Breukels' equations. (b) Element length limit investigation of a beam with $d = 0.25$ m and $p = 0.7$ bar, showing deflection errors compared to element lengths.

6

Structural kite model

This chapter describes how the methodology presented in Chapter 5 is applied to the TU Delft V3 kite. The model is set up from the V3 kite CAD files. The result is a FEM that represents the physical kite, which can be used for structural and aero-structural analysis. The process is applicable to any LEI kite. First, Section 6.1 describes how the model was set up from the design geometry of the kite. Then, in Section 6.2 the approach to distributing the mass of the kite onto the structural model nodes is discussed. Lastly, Section 6.3 shows the test setup used for validating the V3 kite model.

6.1. Model setup

The modelling limitations of the PSM have led previous authors to develop a simplified kite model. While the model does not capture bending stiffness, the model has been proven to be useful in FSI modelling of the kite [36, 37]. As such, the PSM modelling approach was ported to the FEM framework and integrated into the aero-structural framework previously used in combination with the PSM model. Having both level of discretisation in the same modelling framework allows for simple switching between the simple and complex version. The simplified model can be seen alongside the complex model in Figure 6.2.

The complex model, including a representation of the inflatable structure, can be seen on the right in Figure 6.2. This model fully captures the complex bridle line system as well as account for the stiffness in the inflatable structure. The model consists of 1095 degrees of freedom, with 97 beam elements and 784 spring elements.

The bridle line attachment points have been projected onto the chord line, to accommodate for simpler meshing across the kite. This ensures that in the initial configuration, each strut is modelled as a straight, discretised, beam. Billowing effects can then be extracted from a deformed state, and the curvature superimposed on the airfoil to find a new airfoil shape.

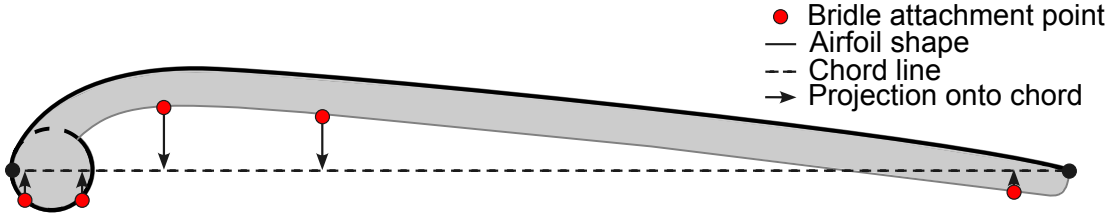

Figure 6.1: Projection of bridle line attachment points onto the chord line

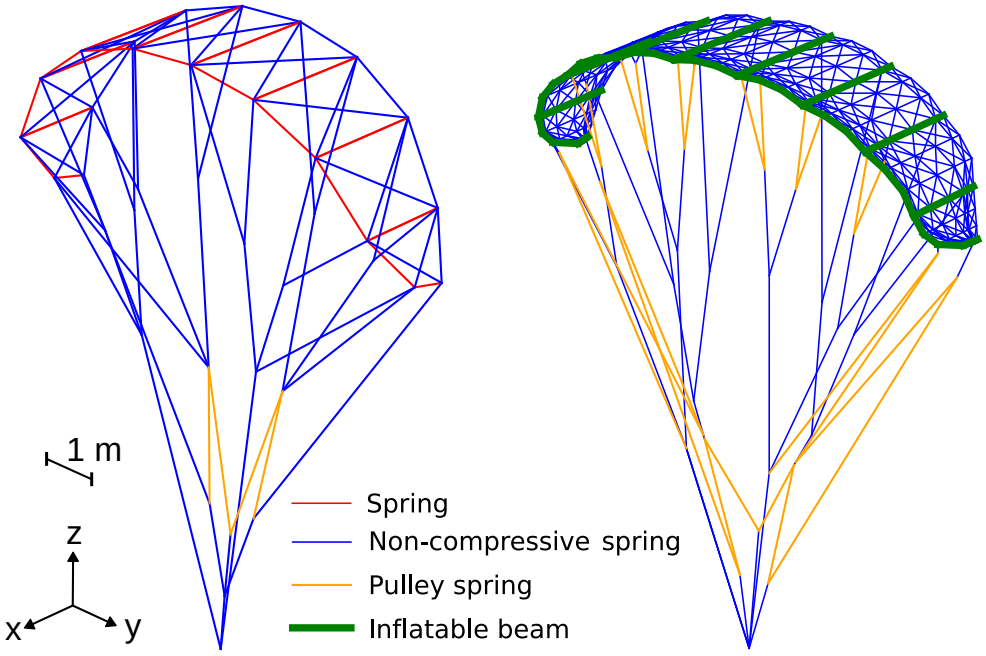

Figure 6.2: Simple V3 kite FEM and complex FEM including inflatable beam structure

The model is meshed based on the CAD geometry from the kite design software Surfplan. This geometry is adapted to a readable format using surfplan adapter [34]. The full V3 bridle plan can also be found in Appendix A. A mesher was written to convert the extracted surfplan geometry to a input that could be used by the finite element modelling framework, the process visualised in Figure 6.3. The mesher also transfers information like line lengths, diameters and tube diameters to the finite element model. The resulting workflow can therefore easily be integrated by kite designers, who design the kite in surfplan, and can then generate a finite element model from the surfplan files along with the required setup to perform a aero-structural simulation. Such a workflow could provide beneficial because it allows for many design iterations to be performed computationally, without needing to produce a physical kite for testing. The full codebase can be found on the repository accompanying this thesis [38].

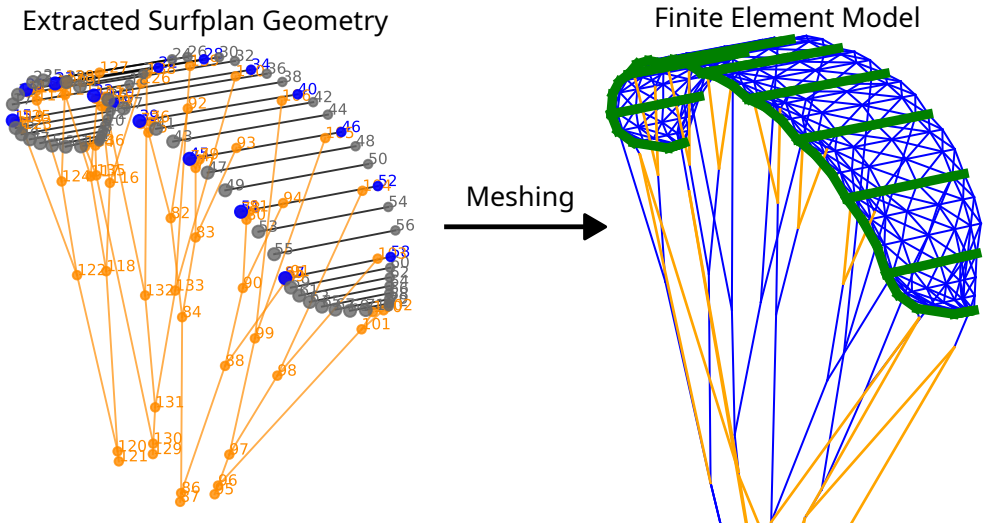

Figure 6.3: Meshing process from surfplan adapter to finite element model.

6.2. Mass distribution

An appropriate mass distribution is required to represent the gravity loading on the kite. The wing, without bridle line system, was weighed at $m_{\text{wing}} = 11\ \text{kg}$. The area density of the canopy material, Dacron, was taken at $\rho_A = 170\ \text{gm}^{-2}$. The surface area of each quadrilateral section consisting of four nodes, A_{quad},as defined in Figure 5.4a, was taken by describing the quadrilateral with two triangles, and calculating the area of those, this ensures that the surface can be calculated if the four nodes are not planar. The mass of a canopy section was then calculated by taking

$$m_{\text{quad}} = \rho_A A_{\text{quad}}. \tag{6.1}$$

Each node in the quadrilateral is then assigned a quarter of this mass. This is repeated for all quadrilaterals, and the mass of all canopy nodes can be summed together to come to the canopy mass m_{canopy}. The inflatable structure mass can then be determined by

$$m_{\text{inflatable}} = m_{\text{wing}} - m_{\text{canopy}}. \tag{6.2}$$

The total length of all beam elements is determined by summing individual lengths. The linear density of the inflatable structure is then given by

$$\rho_L = \frac{m_{\text{inflatable}}}{\sum_{i=0}^{n_{beams}} L_i}. \tag{6.3}$$

Then for each beam element the mass is determined with

$$m_{\text{beam}} = \rho_L L_{\text{beam}}, \tag{6.4}$$

and the mass distributed equally among both nodes of the element. This approach does disregard that the diameter of the inflatable tubes are not the same throughout the wing, and therefore is only a crude approximation. lastly, the mass of the bridle line structure was determined by calculating the mass of each line using the density of Dyneema $\rho = 724\ \text{gm}^{-3}$, length L and diameter d,

$$m_{\text{line}} = \frac{\rho d^2 L_{\text{line}}}{4}. \tag{6.5}$$

Again, the mass is distributed equally among both nodes. For nodes describing a pulley, an additional $100\ \text{g}$ of mass is added. The above procedure leads to a total kite mass of $14\ \text{kg}$, distributed along the kite model.

6.3. Hanging test setup

In order to validate the model, tests are performed where the kite is hung upside down in a hangar, devoid of any aerodynamic loading. The kite is purely subjected to its own gravity and certain enforced loadings. This ensures that the FEM can be validated without any uncertainties added by including an aerodynamic analysis. The hanging test was performed in collaboration with Haanen [17], using stereoscopic camera measurements to determine the kite's shape. The basics of the measuring method is introduced here, for full detail the reader is referred to [17].

Two cameras were mounted in the kite's bridle line system. Depth is perceived similarly to how depth is perceived by a pair of eyes. A single eye can not be perceive depth but a combination of two eyes can. The combination of two camera's can determine the depth of a marker as schematically shown in Figure 6.4. The method works on the principle of triangulation. The two cameras are mounted on a bar with fixed distance B. The angles Θ_A and Θ_B can be determined and then the distance z can be calculated using

$$z = B\frac{\sin(\Theta_A)\sin(\Theta_B)}{\sin(\Theta_A + \Theta_B)}. \tag{6.6}$$

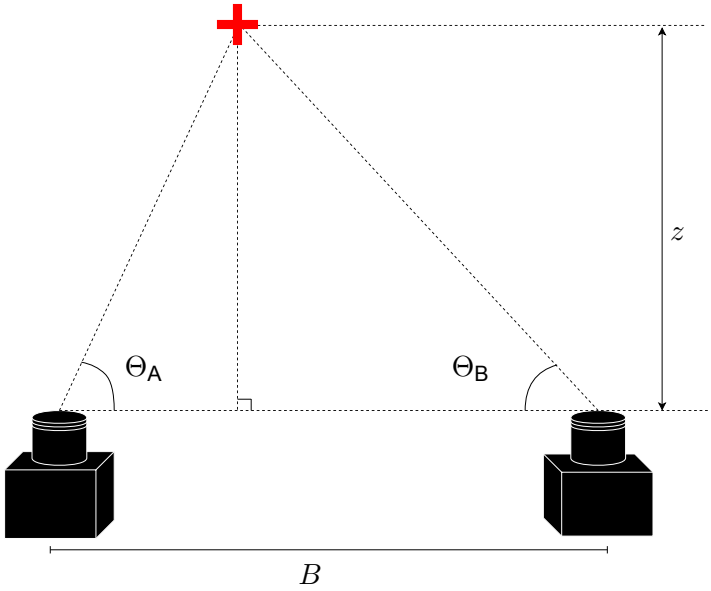

Figure 6.4: Stereographic depth perception based on triangulation of two cameras [17].

The markers are placed onto the inflatable structure, on the locations seen in Figure 6.6, where the distance of each marker can be determined, and a three-dimensional wireframe can be constructed. Theses measurements provide a dataset that can be used to validate the FEM.

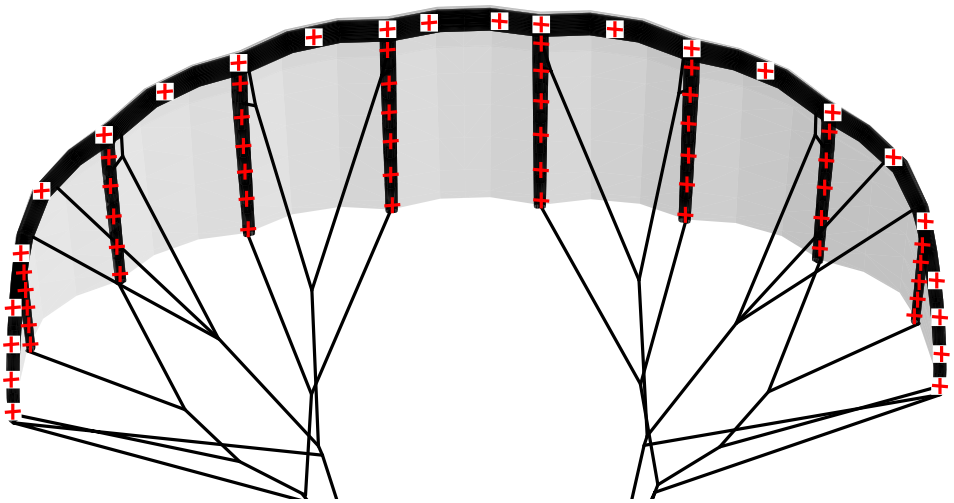

Figure 6.5: Marker placement on the V3 kite for obtaining stereoscopic deformation measurements [17]

The bridle line system of the V3 kite was adapted slightly to fit within the height limit of the hangar. The resulting bridle geometry can be found in Appendix C. The FEM bridle lines were adapted accordingly to represent the hanging test setup. Three characteristic lengths were determined, that would act as a quantitative comparison between kite model and measurements. The three lengths, defining the span, trailing edge length, and the distance between the centre leading edge and tip, can be seen in Figure 6.6. The pressure of the kite could be varied and two possible loading cases were determined. The kite could be loaded in the centre by placing a weight, or the tips could be pulled apart with ropes and the force determined using a load cell. Both load cases are also shown in Figure 6.6.

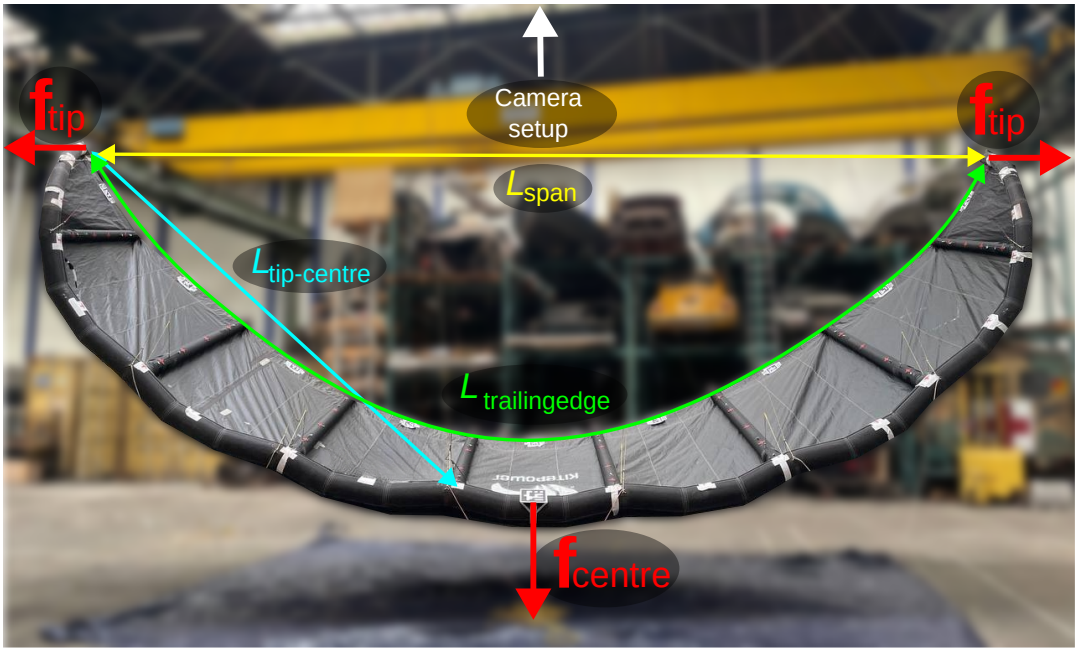

Figure 6.6: Static testing setup of the V3 Kite under gravity load, indicating applied tip and centre loading as well as lengths used for validation.

7

Results

This chapter presents the results obtained with the developed finite element model applied to the TU Delft V3 kite. Section 7.1 presents validation of the structural response against the static tests. Section 7.2 demonstrates how the model resolves slack lines in the bridle and structural system, a feature of direct relevance to kite design and load-path analysis. Then, Section 7.3 shows that canopy billowing can be extracted from the finite element results, enabling future aero-structural model development that accounts for deformation-induced aerodynamic effects. Lastly, Section 7.4 shares preliminary results of the structural model integrated within the aero-structural framework.

7.1. Validation

The hanging kite model was subjected to the ten different load cases (LC) as defined in Table 7.1. The model was run to convergence, and the element stiffnesses were adjusted so that each element's elongation remained below 1%. The model results of the three main loading types, gravity, centre, and tip loading, for both pressures can be seen in Figure 7.1.

Table 7.1: Validation test cases, with varying pressure and applied loads.

Load case		1	2	3	4	5	6	7	8	9	10
Pressure	(bar)	0.15	0.15	0.15	0.15	0.15	0.25	0.25	0.25	0.25	0.25
centre load	(N)	0	95	247	0	0	0	95	247	0	0
Tip load	(N)	0	0	0	20	49	0	0	0	20	49

The load cases with only gravity loading, one and six, show the kite in a compact state with the tips curling inwards. The canopy is sagging, which looks similar to billowing although sagging is not due to aerodynamic effects. The distance between the struts at the trailing edge is reduced, resulting in a lower span. Under increased pressure in LC6, one can see that the inflatable structure indeed shows increased stiffness, resulting in a slightly increased span.

LC3 and LC8 are subject to a vertical load in the centre. This has the effect of tilting the kite forwards by fully loading the front centre bridles. Furthermore, the two centre struts show a large inclination, with the trailing edge pointing upwards. Compared to the gravity loaded case, the tips have folded out and the span has increased. This is a counter-intuitive result, as one would expect the tips to fold inwards. Some billowing is apparent in the canopy and no large change is seen when increasing the pressure.

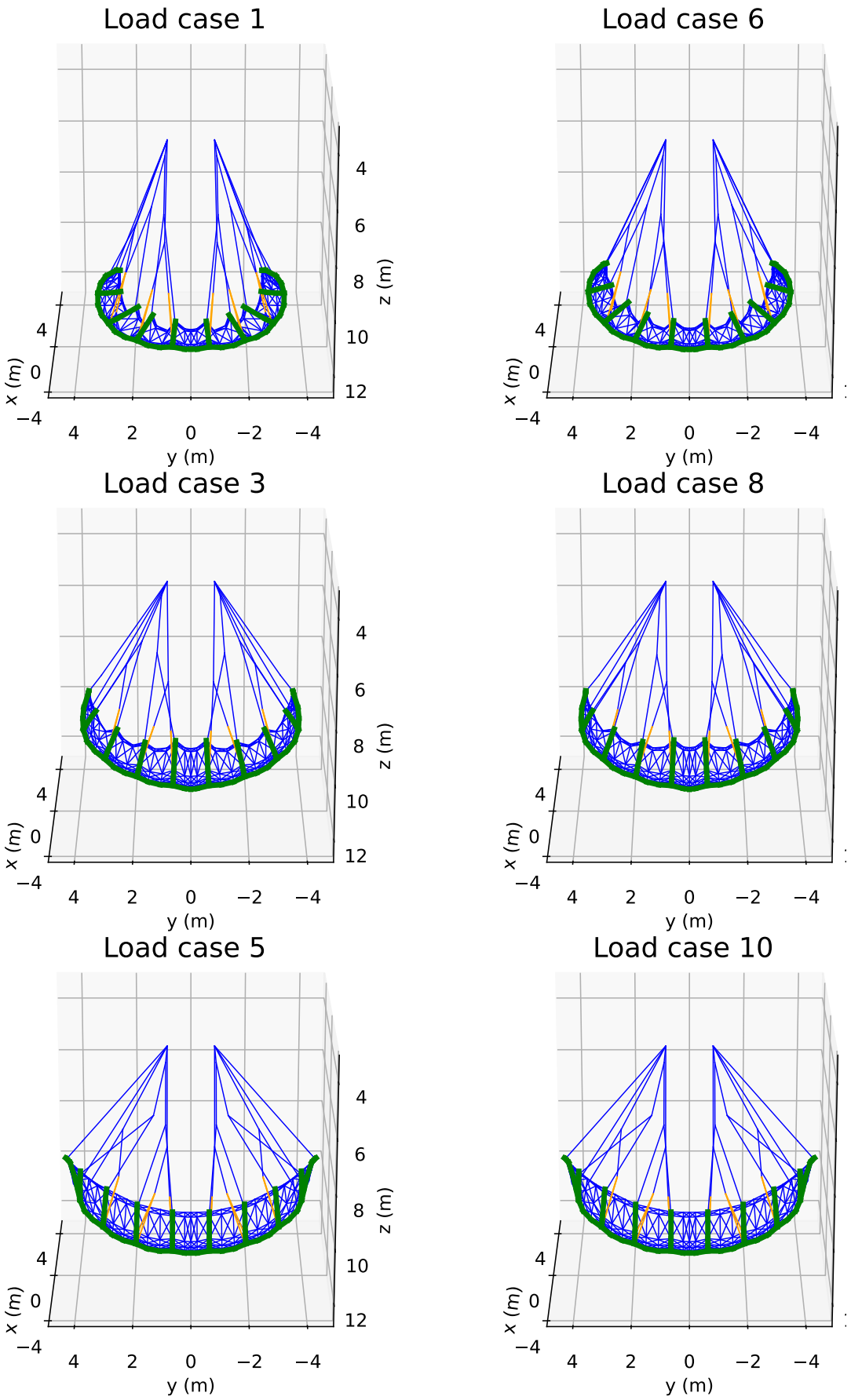

Figure 7.1: Finite element results of the V3 kite modelled under gravity loading, centre loading and tip loading for two different pressures.

The results of the model cases with tip loading, seen in LC5 and LC10. Show the kite with a large span, where the canopy is fully stretched. In the bridle lines some strange orientations are found, caused by slack lines which is further discussed in Section 7.2. The deformation looks as expected from the input loading, and little difference is seen when increasing the pressure.

The model results were compared with the stereoscopically obtained measurements, and the characteristic lengths defined in Figure 6.6 were compared to assess model accuracy quantitatively. The results are shown in Table 7.2, where the errors are presented as well as the relative error. The errors are defined as

$$\epsilon = L_{\text{model}} - L_{\text{exp}}, \tag{7.1}$$

and the relative errors as

$$\varepsilon = \frac{\epsilon}{L_{\text{exp}}} \cdot 100\%. \tag{7.2}$$

The average error is defined as the average of the absolute values of the three percentages.

The centre-loaded cases show large errors in the estimated span and trailing-edge length. From the results in Figure 7.1 it was already concluded that this folding out of the tips compared to the gravity only case is a counter-intuitive result. It is likely that by applying such a local load directly on the inflatable beam, the cross-section deforms and the stiffness of the tube reduces. The simplification made by modelling such a complex structure as a beam element cannot capture this and therefore is unable to resolve the shape.

The gravity only and tip loading cases however, show a good correspondence between model results and measurements, with the average error between below 6.2%. The span is overstated in every case. This could be partly explained by the tuning of the bridle lines' stiffnesses to ensure elongation is limited to 1%. This can cause all the bridle lines to slightly stretch, leading to an overestimation of the span.

Table 7.2: Errors and relative errors of characteristic lengths for the various static load cases.

Load case		1	2	3	4	5	6	7	8	9	10
Trailing-edge error	(m)	-0.2	1.5	1.3	0.7	0.6	-0.1	1.2	1.1	0.6	0.6
Span error	(m)	0.2	2.1	2.2	0.5	0.6	0.5	1.8	1.8	0.6	0.7
Tip-centre error	(m)	-0.5	0.5	0.4	0.2	0.1	-0.1	0.4	0.3	0.1	0.2
Trailing-edge error	$(\%)$	-1.9	19.1	14.9	7.1	6.1	-1.0	13.7	12.6	5.6	6.1
Span error	$(\%)$	4.4	40.8	43.7	7.0	7.6	9.1	31.4	30.9	7.3	8.2
Tip-centre error	$(\%)$	-11.6	12.2	9.7	4.4	2.9	-3.0	9.3	7.8	3.0	4.0
Average error	$(\%)$	6.0	24.1	22.8	6.2	5.5	4.3	18.1	17.1	5.3	6.1

A more qualitative comparison is made by overlaying the inflatable structure of the model with measured shape. All load cases are compared in Figure 7.2. These visualisations are in good agreement with the results found in Table 7.2. The inflatable structures of all load cases with gravity and tip load cases align well, and the centre loading cases do not. The alignment of struts is off in all cases, however this is also caused by the cross-section simplification made in Figure 6.1

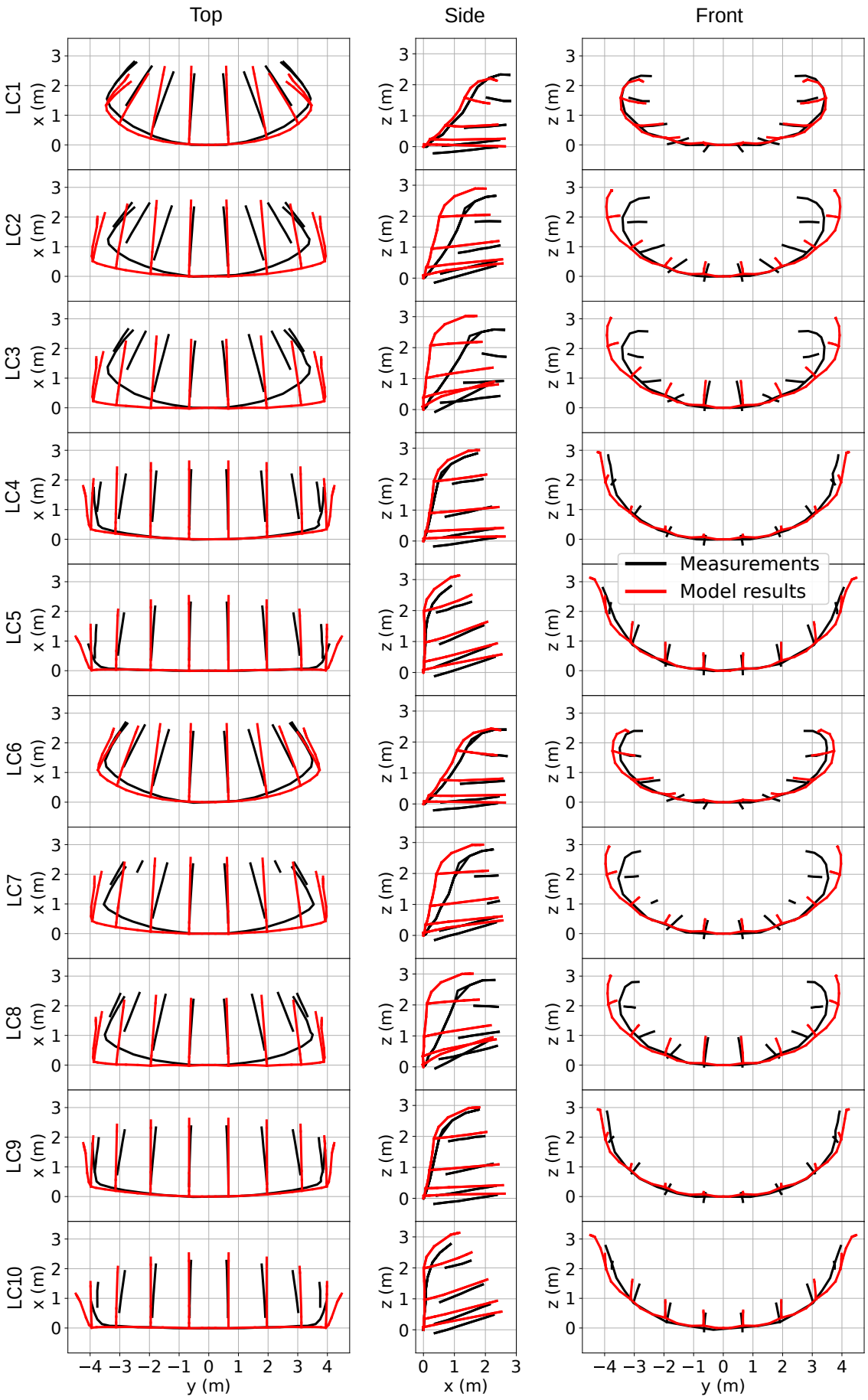

Figure 7.2: Inflatable structure comparisons between measurements and modelling results

7.2. Slack line analysis

The modelling approach allows for some further interesting analysis. The elongation of each bridle line can be checked in order to investigate the effectiveness of the bridle configuration. While not of particular interest in the case of the static, hanging kite, such information allows for simulating a kite in flight and checking if the bridle lines are slack or tensioned. This could be a helpful tool for kite or bridle designers. In Figure 7.3 one can see the strain of each line for load case five. Most of the rear bridle lines are slack, and the loads are mainly transferred through the rear bridle lines at the tip and the front bridles.

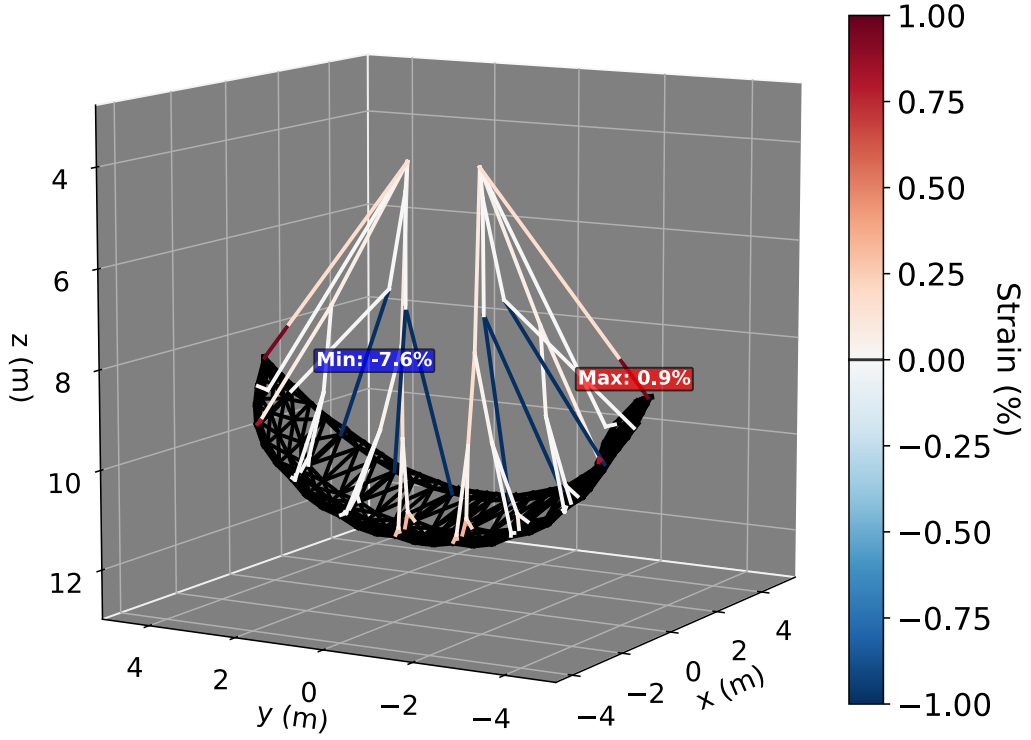

Figure 7.3: Element strain of the hanging kite under load case 5, with blue indicating slack lines or elements

7.3. Billowing effects

Due to the deformation on the kite, the airfoil cross-sections change. Under aerodynamic loads, the canopy gets inflated and starts to billow, the trailing edges of the struts move closer together and the span decreases. For proper aerodynamic analysis, it is important that this change in airfoil is captured. The finite element modelling approach allows for the extraction of new airfoil shapes. In the hanging test case, the canopy sags causing a similar effect to billowing. In Figure 7.4, three cross sections are extracted from the kite in hanging condition. The cross-sections are nondimensionalised with the chord length. This billowing effect can be superimposed on the airfoil shape to determine an updated airfoil shape to use for aerodynamic analysis. Such an extraction of billowing properties was not possible before using the PSM approach, and this added fidelity allows for more detailed aero-structural modelling.

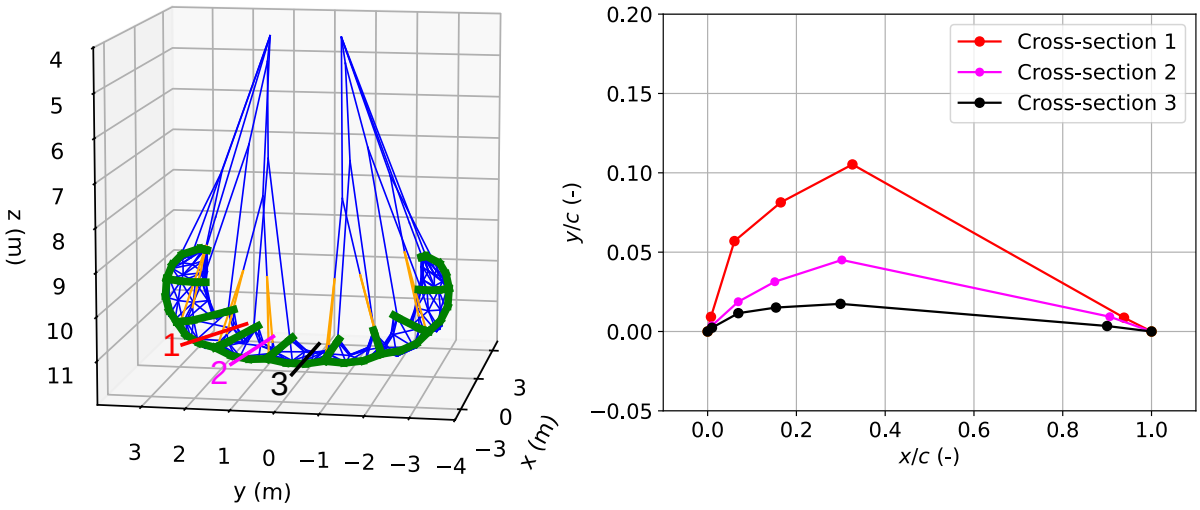

Figure 7.4: Extracted billowing effects on three cross-sections of the kite in load case 1.

7.4. Preliminary aero-structural results

The model has been partly integrated into the aero-structural framework by Poland and Cayon [37, 36, 8], which was explained in Section 4.1. At the time of writing, a single iteration loop could be simulated. Based on the initial wind direction, coming from the x direction, the aerodynamic loading was determined using the VSM. Together with the gravity loading the external force vector was determined and applied onto the structural model. Figure 7.5 shows the resulting kite orientation and shape after one aero-structural iteration loop.

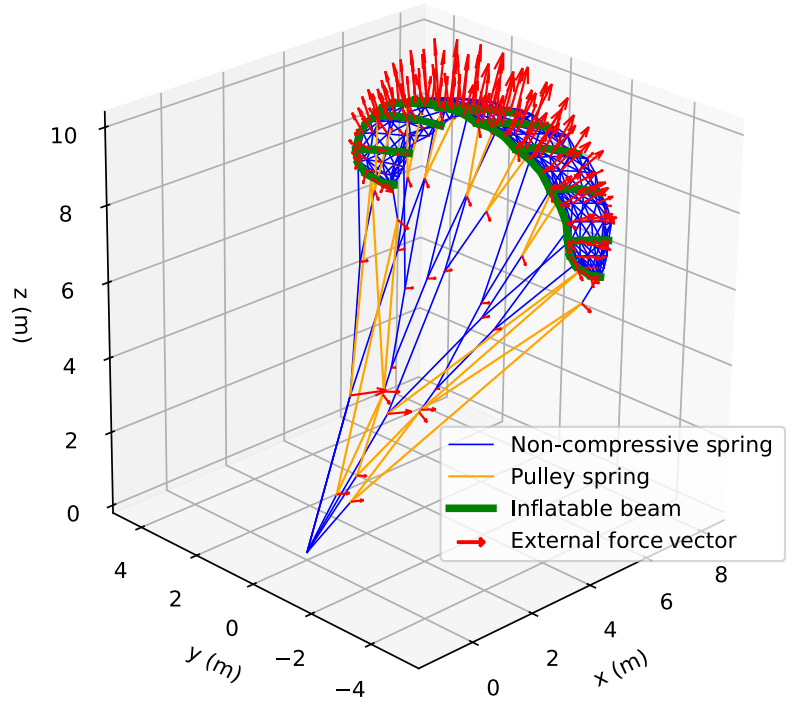

Figure 7.5: Kite shape and orientation under aerodynamic and gravity loading after aero-structural simulation iteration

8

Conclusions

This thesis set out to determine a modelling approach that enables a computationally efficient structural model for LEI kites, capturing the inflatable structure's bending and torsional stiffness. This objective was pursued by first determining a trade-off between candidate models and subsequent development and validation of a reduced, geometrically non-linear finite element model.

The comparison between a PSM beam representation and a FEM beam representation demonstrates that, although both approaches are capable of modelling beam bending, the particle system approach becomes impractical when applied to a kite. Representing a beam within a PSM requires a high amount of degrees of freedom and spring elements, leading to an increased computational cost. The approach is therefore considered unsuitable for applying to a LEI kite. In contrast, the non-linear finite element approach has shown to be a effective way to describe a kite's inflatable beams at a much lower computationally cost. The beam elements can be tuned to represent physical inflatable beam behaviour, as measured by Breukels [6], and were shown to line up with measurements. The finite element framework is subsequently also suitable for resolving the bridle line system, due to the co-rotational framework. To the author's knowledge, this is the first time that both the bridle line system and wing are resolved in a singular structural model.

The approach to integrating the FEM structural framework into a large aero-structural model has been discussed and the model inputs and outputs were determined such that it could swap into place in the existing aero-structural framework by Poland [37]. The first steps were taken, with the existing simplified PSM being represented in the FEM framework, and integrated into to aero-structural solver. The complete FEM, as described in this work, remains to be fully integrated into the aero-structural framework, with only single iteration simulations performed so far.

The kite model resulting from this work has an increased fidelity compared to the previous PSM approach. With the representation of the inflatable structure, deformations like jelly fishing and bunny-ear can be resolved, though the effect can likely only be shown in an aero-structural coupled simulation. The representation of the inflatable structure also allows for increased canopy discretisation, enabling resolving the billowing effects. Leading-edge indentation and collapse are both deformations that are closely related to failure, and therefore trying to resolve these might be difficult due to numerical instabilities within the aero-structural framework. Subscale deformations can not be modelled at all as these require a unsteady modelling approach,

while this framework has focussed on a quasi-steady modelling approach.

The FEM of the V3 kite was validated against stereoscopically obtained deformation data of the kite hanging upside down. Various loads were applied, the kite pressures was varied and the resulting comparison between model and measurements showed good correspondence for most cases. In the case were a perpendicular load was locally applied at the centre of the leading edge, the model was not able to capture the resulting deformation. Such a local perpendicular load would deform the shape of the leading edge, and therefore the bending stiffness due to the internal pressure would decrease. Such deformations can not be captured in the simplified two node beam approximation. In flight, the kite deals with a distributed loading and therefore the model should be applicable here. In all other cases the model predicted the resulting kite shape rather well.

Concluding, the thesis has established that a reduced non-linear finite element approach, using tuned Timoshenko beam elements to represent the inflatable structure, is an effective solution for modelling LEI kites' structural behaviour within an aero-structural framework. The developed method strikes a balance between capturing dominant structural behaviour, while keeping computational cost low. The model can be integrated into a aero-structural solver and can be used as a tool to asses kite performance computationally, rather than through testing.

9

Recommendations

The developed structural model successfully captures the dominant deformation behaviour of leading-edge inflatable kites, and can be used within a quasi-steady aero-structural framework. However, the author notes several key improvements.

First of all, the system is solved using a Newton-Raphson iteration scheme, which falls under the stiffness matrix method of form finding problems. PSM literature has shown that dynamic methods, including mass and damping matrices, can be beneficial in terms of stability and potentially solver time. The current Newton-Raphson approach does seem to be relatively stable, however solving the V3 kite model can take up to 10 minutes. Since the dynamic methods work rather well for PSM, such a solver should be investigated for the FEM approach as well, potentially improving stability and solver time.

Another improvement in solver time could be made by applying the aerodynamic loads as follower forces on the kite. This means that the forces will rotate to be perpendicular to the canopy surface. Implementing this will ensure that fewer iterations are required between structural and aerodynamic solver.

Furthermore, the current use of tuned Timoshenko beam elements works for the V3 kite case. however, as the length limit investigation has shown that the elements should not be longer than two meters, larger kites might become unnecessarily discretised causing more computational time. Ideally, the same kite model can be scaled up to larger sizes such that the effects of a larger kite can easily be analysed. In its place, one could fit Timoshenko beam elements that are specifically derived to represent inflatable structures, such as [26], which allows for a more physical representation, rather than tuning beam properties to match measurements.

The physicality of the model can be further improved by removing the cross-section simplification that projects all bridle line attachment points onto the chord line. This was implemented because the inflatable structures in real life are three-dimensional tubular shapes. In the finite element representation, they are simply a line. Therefore, the nodes describing the attachment points and the nodes describing the inflatable structures do not coincide. This could potentially be resolved by describing a way in which these nodes are constrained, such as fixing the attachment point with to the centre of the beam with a prescribed radius. Using such ”rigid links”, one can potentially remove the simplification in cross-section which results in a more physical representation of the kite, and reduces interfacing between aerodynamic and structural solver.

Lastly, the recommendation is to start using the v3 kite model in further research. The framework can be found in the codebase accompanying this thesis [38]. The next step would be to finish the integration of the model into the aero-structural solver by Poland [37], for which the first steps have already been taken. Billowing effects can then also be resolved by using the airfoil regression model by Masure [31]. The aero-structural model can once again be validated using flight data obtained by Haanen [17]. A complete aero-structural model can then be used to investigate steering behaviour, deformation effects during the flight path, and kite scaling effects. Furthermore the toolchain can also be used by kite designers to fly their designs virtually, and to investigate performance before committing to a kite design.

References

[1] M. R. Barnes. “Form finding and analysis of tension space structures by dynamic relaxation”. City University London, Oct. 1977. URL: https://openaccess.city.ac.uk/id/eprint/11887/ (visited on 06/07/2025).

[2] A. R. Batchelor. “Development and benchmarking of a Particle System framework for structural modeling of soft-wing kites” (2023). URL: https://repository.tudelft.nl/record/uuid:42bd7d60-de62-4e11-ad73-5468144aaf59 (visited on 03/12/2025).

[3] J. Berens. “Dynamic Nonlinear Aeroelastic Behaviour of Flexible Wings in an Airflow” (2015). URL: https://repository.tudelft.nl/record/uuid:aa859e12-1087-46a5-80c6-7e63053a017a (visited on 05/01/2025).

[4] H. A. Bosch. “Finite Element Analysis of a Kite for Power Generation” (2012). URL: https://repository.tudelft.nl/record/uuid:888fe64a-b101-438c-aa6f-8a0b34603f8e (visited on 04/24/2025).

[5] J Breukels and Wubbo Ockels. “Analysis of complex inflatable structures using a multibody dynamics approach” (2008). URL: https://repository.tudelft.nl/record/uuid:82a736f6-c4fa-467a-a6f1-78b88620962b (visited on 08/27/2025).

[6] J. Breukels. “An engineering methodology for kite design”. 2011. URL: https://repository.tudelft.nl/record/uuid:cdece38a-1f13-47cc-b277-ed64fdda7cdf (visited on 03/18/2025).

[7] Saullo G. P. Castro. *General-purpose finite element solver based on Python and Cython*. Oct. 2024. DOI: 10.5281/ZENODO.6573489.

[8] Oriol Cayon, Mac Gaunaa, and Roland Schmehl. “Fast Aero-Structural Model of a Leading-Edge Inflatable Kite” (Jan. 2023). P. 3061. DOI: 10.3390/en16073061.

[9] R. L. Comer and Samuel Levy. “Deflections of an inflated circular-cylindrical cantilever beam” (July 1963). Pp. 1652–1655. DOI: 10.2514/3.1873.

[10] Pieter-Jan Declercq. “Analyse van het aero-elastisch gedrag van een flexibele vlieger voor windenergie” (2022). URL: http://lib.ugent.be/catalog/rug01:003063362.

[11] Uwe Fechner et al. “Dynamic model of a pumping kite power system” (Nov. 2015). Pp. 705–716. DOI: 10.1016/j.renene.2015.04.028.

[12] Carlos Felippa. “A Systematic Approach to the Element-Independent Corotational Dynamics of Finite Elements” (Jan. 2000).

[13] Mikko Folkersma, Roland Schmehl, and Axelle Viré. “Steady-state aeroelasticity of a ram-air wing for airborne wind energy applications” (Sept. 2020). P. 032018. DOI: 10.1088/1742-6596/1618/3/032018.

[14] Allister Furey and Inman Harvey. “Evolution of Neural Networks for Active Control of Tethered Airfoils” (2007). Pp. 746–755. DOI: 10.1007/978-3-540-74913-4_75.

[15] N. H. Geschiere. “Dynamic modelling of a flexible kite for power generation” (2014). URL: https://repository.tudelft.nl/record/uuid:6478003a-3c77-40ce-862e-24579dcd1eab (visited on 04/24/2025).

[16] F. J. J. M. M. Geuskens. “Conformable Pressurized Structures” (2012). URL: https://repository.tudelft.nl/record/uuid:67fa0d80-98a9-4041-8d68-29a3ada4bd2a (visited on 04/28/2025).

[17] P.J. Haanen. “In-flight experimental measurements of large-scale deformations on a leading-edge inflatable kite”. J. Phys.: Conf. Ser. (2026).

[18] R. B. Haber and J. F. Abel. “Initial equilibrium solution methods for cable reinforced membranes part I—formulations” (June 1982). Pp. 263–284. DOI: 10.1016/0045-7825(82)90080-9.

[19] J A W Poland. “Modeling aeroelastic deformation of soft wing membrane kites” (2022). DOI: 10.13140/RG.2.2.27851.92967.

[20] M. C. Karadayi. “Particle System Modelling and Dynamic Simulation of a Tethered Rigid Wing Kite for Power Generation” (2016). URL: https://repository.tudelft.nl/record/uuid:d6a2fcf8-7fce-4eb8-857b-209b9faac755 (visited on 03/18/2025).

[21] E. F. van der Knaap. “A particle system approach for modelling flexible wings with inflatable support structures” (2013). URL: https://repository.tudelft.nl/record/uuid:c77c5c6a-0bf7-47d5-b5bf-c5efac0c2d83 (visited on 03/12/2025).

[22] B. Lansdorp, P. D. Williams, and Wubbo Ockels. “Flexibel Tethered Kite with Moveable Attachment Points Part I: Dynamics and Control” (2007). URL: https://repository.tudelft.nl/record/uuid:e5e25332-aa49-41fc-ab6b-1ea13a0027a5 (visited on 04/29/2025).

[23] B. Lansdorp, P. D. Williams, and Wubbo Ockels. “Flexible Tethered Kite with Moveable Attachment Points Part II: State and Wind Estimation” (2007). URL: https://repository.tudelft.nl/record/uuid:99fcf865-f4e0-4e64-8fe7-389e283c7d8c (visited on 04/29/2025).

[24] Bas Lansdorp et al. “Modeling, Simulation, and Testing of Surf Kites for Power Generation”. *AIAA Modeling and Simulation Technologies Conference and Exhibit*. Guidance, Navigation, and Control and Co-located Conferences. American Institute of Aeronautics and Astronautics, Aug. 2008. DOI: 10.2514/6.2008-6693.

[25] A. Le Van and C. Wielgosz. “Bending and buckling of inflatable beams: Some new theoretical results”. en (Aug. 2005). Pp. 1166–1187. DOI: 10.1016/j.tws.2005.03.005.

[26] Anh Le Van and Christian Wielgosz. “Finite element formulation for inflatable beams” (Feb. 2007). Pp. 221–236. DOI: 10.1016/j.tws.2007.01.015.

[27] Rachel Leuthold. “Multiple-Wake Vortex Lattice Method for Airborne Wind Energy Membrane-Wing Kites” (2015). URL: https://repository.tudelft.nl/record/uuid:bad76ade-81d3-4d86-a631-c45319812445 (visited on 08/27/2025).

[28] Miles L. Loyd. “Crosswind kite power (for large-scale wind power production)” (1980). Pp. 106–111. DOI: 10.2514/3.48021.

[29] Yunhua Luo. “An efficient 3D Timoshenko beam element with consistant shape functions” (Oct. 2008). Pp. 95–106.

[30] Kirk Martini. “A Particle-System Approach to Real-Time Non-Linear Analysis” (). URL: https://www.academia.edu/29793801/A_Particle_System_Approach_to_Real_Time_Non_Linear_Analysis (visited on 06/10/2025).

[31] Kasper Masure. “Regression Model of Leading Edge Inflatable Kite Profile Aerodynamics”. en (2025). URL: https://repository.tudelft.nl/record/uuid:865d59fc-ccff-462e-9bac-e81725f1c0c9 (visited on 01/27/2026).

[32] Kjell Mattiasson. “Numerical results from large deflection beam and frame problems analysed by means of elliptic integrals” (1981). Pp. 145–153. DOI: 10.1002/nme.1620170113.

[33] Thouraya Nouri-Baranger. “Computational methods for tension-loaded structures” (June 2004). Pp. 143–186. DOI: 10.1007/BF02905937.

[34] Jelle Poland, Tom Mooijman, and Corentin Tan. *SurfplanAdapter*. 2025. URL: https://github.com/jellepoland/SurfplanAdapter.

[35] Jelle Poland and Roland Schmehl. *TUDELFT_V3_KITE*. Mar. 2025. URL: https://awegroup.github.io/TUDELFT_V3_KITE/.

[36] Jelle A. W. Poland and Roland Schmehl. “Modelling Aero-Structural Deformation of Flexible Membrane Kites” (Jan. 2023). P. 5264. DOI: 10.3390/en16145264.

[37] Jelle Agatho Wilhelm Poland and Roland Schmehl. “A virtual wind tunnel for deforming airborne wind energy kites” (June 2024). P. 072001. DOI: 10.1088/1742-6596/2767/7/072001.

[38] Patrick Roeleveld. *kite_fem*. 2026. URL: https://github.com/awegroup/kite_fem (visited on 01/23/2026).

[39] Saman Sabzehzar et al. “Proposing a practical equivalent Timoshenko beam for analysis of truss structures” (May 2024). P. 106401. DOI: 10.1016/j.istruc.2024.106401.

[40] Roland Schmehl. *Airborne Wind Energy*. June 2019. URL: http://awesco.eu/awe-explained/ (visited on 05/23/2025).

[41] J. F. J. E. M. Schwoll. “Finite Element Analysis of Inflatable Structures Using Uniform Pressure” (2012). URL: https://repository.tudelft.nl/record/uuid:f92da57f-55df-4109-9f8a-8c7c2b220c6a (visited on 03/18/2025).

[42] Alain de Solminihac et al. “Kite as a Beam: A Fast Method to get the Flying Shape”. *Airborne Wind Energy*. Springer, Singapore, 2018, pp. 79–97. DOI: 10.1007/978-981-10-1947-0_4.

[43] *SurfPlan*. URL: http://www.surfplan.com.au/sp/default.aspx (visited on 02/12/2026).

[44] Lip H. Teh and Murray J. Clarke. “Co-rotational and Lagrangian formulations for elastic three-dimensional beam finite elements” (Nov. 1998). Pp. 123–144. DOI: 10.1016/S0143-974X(98)00200-4.

[45] P. Thedens. *A membrane finite element solver based on kinetic dynamic relaxation*. June 2022. URL: https://github.com/pthedens/mem4py (visited on 03/24/2025).

[46] P. Thedens. “An integrated aero-structural model for ram-air kite simulations: with application to airborne wind energy”. Delft University of Technology, 2022. DOI: 10.4233/UUID:16E90401-62FC-4BC3-BF04-7A8C7BB0E2EE.

[47] Jelte van Til et al. “Dynamic Model of a C-shaped Bridled Kite Using a few Rigid Plates”. *Airborne Wind Energy*. Springer, Singapore, 2018, pp. 99–115. DOI: 10.1007/978-981-10-1947-0_5.

[48] D. Veenendaal and P. Block. “An overview and comparison of structural form finding methods for general networks” (Dec. 2012). Pp. 3741–3753. DOI: 10.1016/j.ijsolstr.2012.08.008.

[49] Sebastiaan Leopold Veldman. “Design and analysis methodologies for inflated beams”. Netherlands: Technische Universiteit Delft (The Netherlands), 2005. URL: https://www.proquest.com/docview/305372243/abstract?sourcetype=Dissertations%20&%20Theses (visited on 04/28/2025).

[50] Rolf van der vlugt et al. “Quasi-steady model of a pumping kite power system” (July 2019). Pp. 83–99. DOI: 10.1016/j.renene.2018.07.023.

[51] Junsong Wang et al. “An active-bending sheltered pathway based on bamboo strips for indoor temporary applications: Design and construction” (May 2024). P. 117863. DOI: 10.1016/j.engstruct.2024.117863.

[52] Christian Wielgosz, Jean-Christophe Thomas, and Pascal Casari. “Strength of Inflatable Fabric Beams at High Pressure” (Apr. 2002). DOI: 10.2514/6.2002-1292.

[53] Qiu Zhang et al. “Development of an active bending temporary corridor based on bamboo strips: preliminary results”. Aug. 2021.

A

TU Delft V3 kite bridle geometry

Table A.1: V3 bridle line lengths and diameters

Front lines			Rear lines		
Line ID	Length (mm)	Diameter (cm)	Line ID	Length (mm)	Diameter (cm)
A_{main}	3903	0.6	M	4856	0.4
A_{I}	3670	0.5	$B_{\text{r,main,e}}$	70	0.2
A_{II}	3360	0.5	$B_{\text{r,main,1}}$	610	0.2
$A_{\text{III}}/B_{\text{r,main,2}}$	11420	0.2	$B_{\text{r,main,2}}/A_{\text{III}}$	11420	0.2
A_1	1860	0.3	$B_{\text{r,I}}$	2333	0.2
A_2	1798	0.3	$B_{\text{r,II}}$	2045	0.2
A_3	1791	0.3	$B_{\text{r,5}}$	12168	0.4
A_4	2877	0.3	$b_{\text{r,1}}$	4407	0.2
ab_1/cd_1	3261	0.2	$b_{\text{r,2}}$	4180	0.2
ab_2/cd_2	3180	0.2	$b_{\text{r,3}}$	4094	0.2
ab_3/cd_3	3076	0.2	$b_{\text{r,4}}$	3550	0.2
a_1/b_1	330	0.2	$a_{\text{5,e}}$	115	0.2
c_1	445	0.2	a_5	278	0.2
d_1	405	0.2	$b_{\text{r,5,e}}$	115	0.2
a_2/b_2	260	0.2	$b_{\text{r,5}}$	1420	0.2
c_2	400	0.2	PL	1600	1.2 $\times$0.15
d_2	375	0.2	SL	2200	1.2 0$\times$0.15
a_3/b_3	325	0.2			
c_3	400	0.2			
d_3	370	0.2			
a_4/b_4	220	0.2			

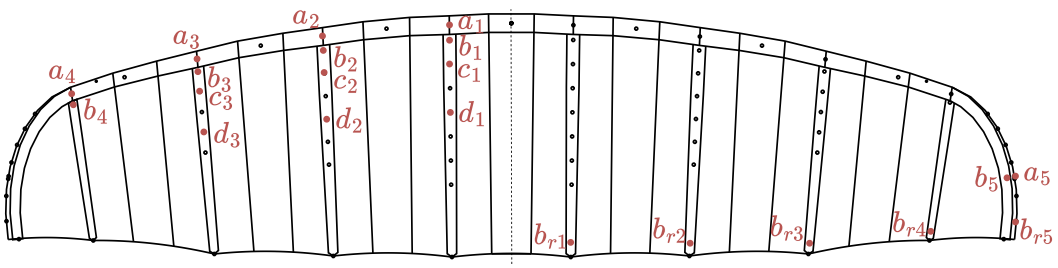

Figure A.1: V3 kite Bridle line attachment points on wing

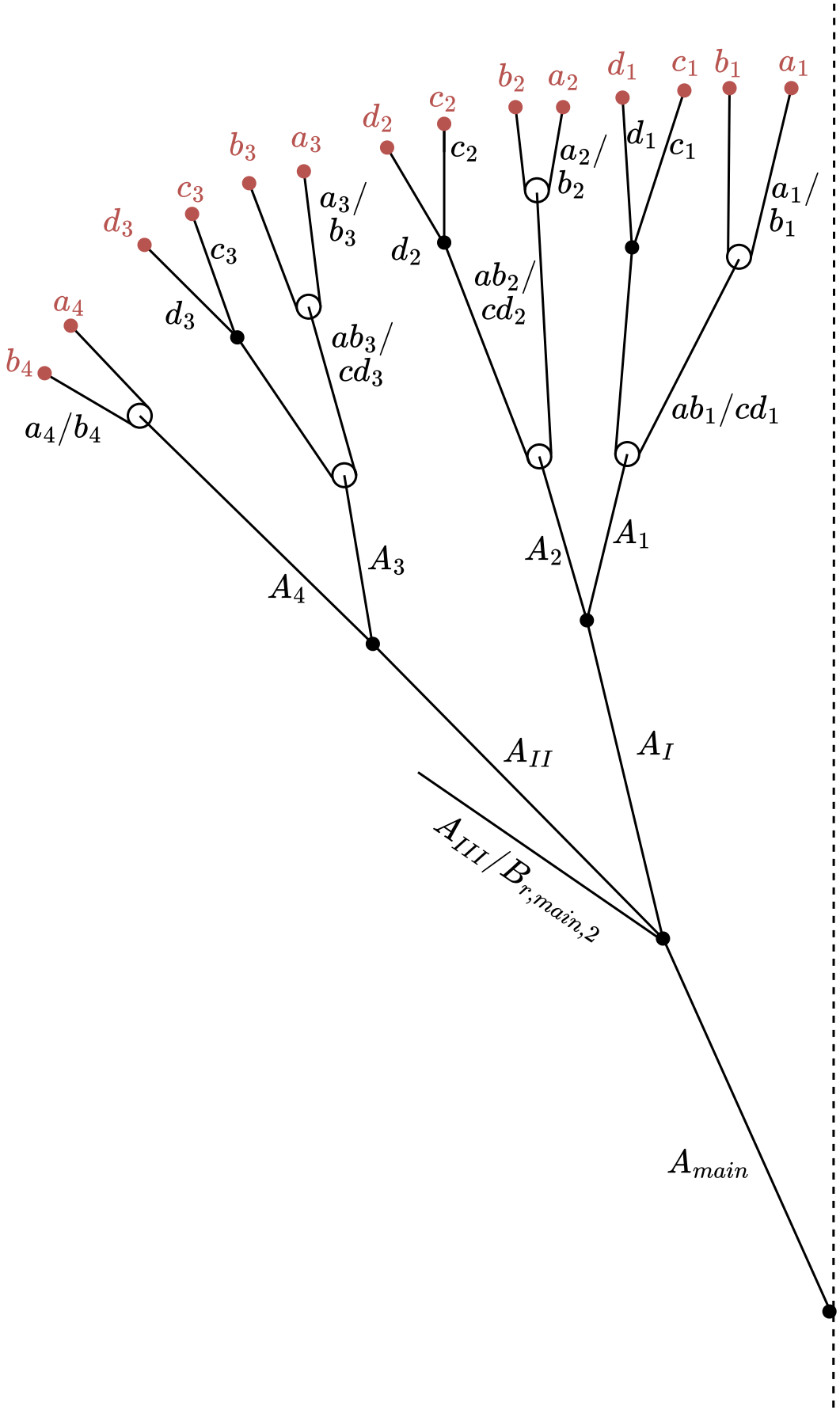

Figure A.2: V3 kite front bridle line geometry, lengths not to scale, figure adapted from [17]

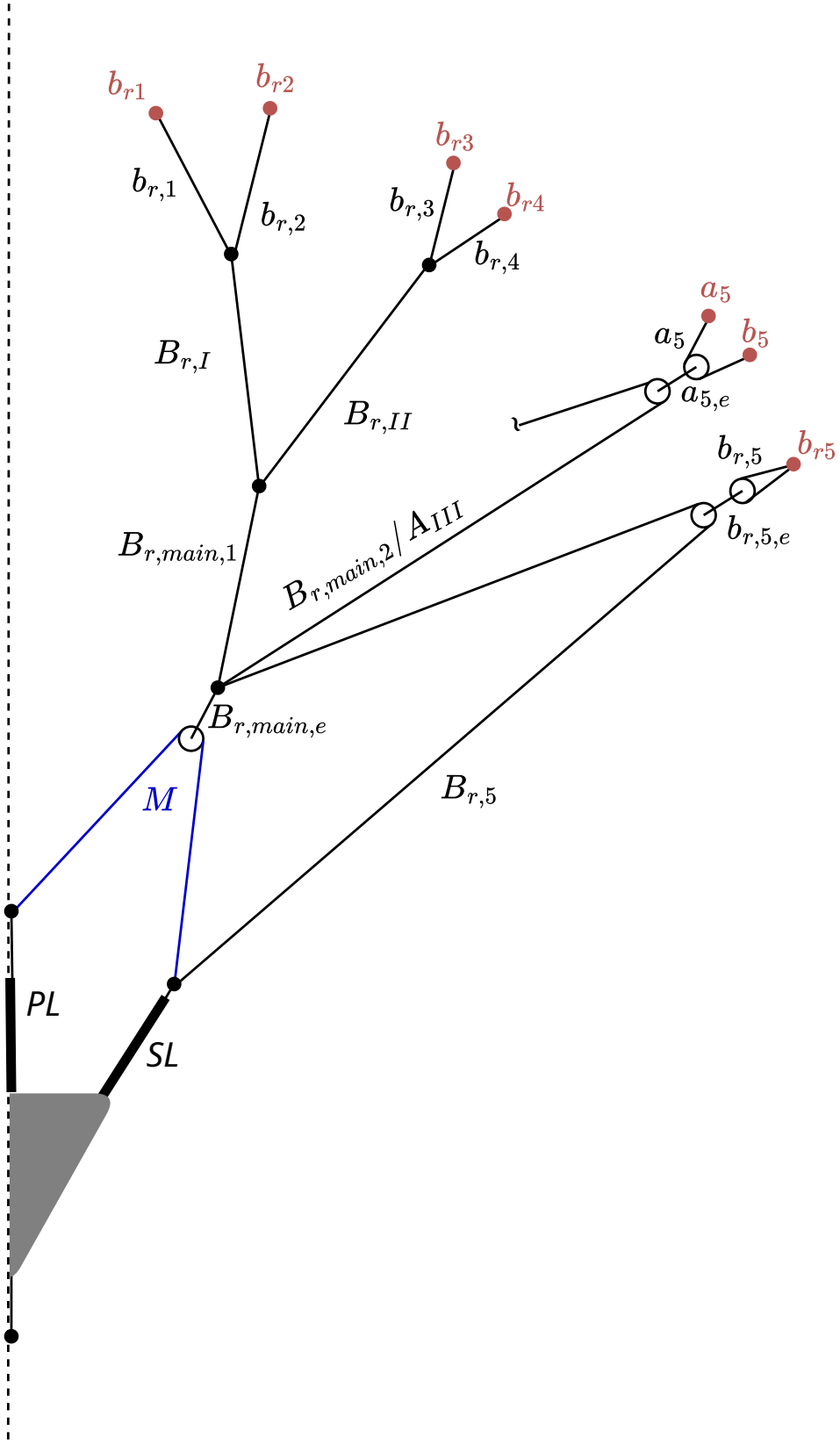

Figure A.3: V3 kite rear bridle line geometry, lengths not to scale, figure adapted from [17]

B

V3 kite hanging test bridle geometry

Table B.1: Adapted V3 bridle line lengths and diameters for hanging test, bold values indicate changes compared to the normal configuration.

Front lines			Rear lines		
Line ID	Length (mm)	Diameter (cm)	Line ID	Length (mm)	Diameter (cm)
A_{main}	**N/A**	0.6	M	**N/A**	0.4
A_{I}	**N/A**	0.5	$B_{\text{r,main,e}}$	70	0.2
A_{II}	3360	0.5	$B_{\text{r,main,1}}$	610	0.2
$A_{\text{III}}/B_{\text{r,main,2}}$	11420	0.2	$B_{\text{r,main,2}}/A_{\text{III}}$	11420	0.2
A_1	1860	0.3	$B_{\text{r,I}}$	2333	0.2
A_2	1798	0.3	$B_{\text{r,II}}$	2045	0.2
A_3	1791	0.3	$B_{\text{r,5}}$	**9425**	0.4
A_4	2877	0.3	$b_{\text{r,1}}$	4407	0.2
ab_1/cd_1	3261	0.2	$b_{\text{r,2}}$	4180	0.2
ab_2/cd_2	3180	0.2	$b_{\text{r,3}}$	4094	0.2
ab_3/cd_3	3076	0.2	$b_{\text{r,4}}$	3550	0.2
a_1/b_1	330	0.2	$a_{\text{5,e}}$	115	0.2
c_1	445	0.2	a_5	278	0.2
d_1	405	0.2	$b_{\text{r,5,e}}$	115	0.2
a_2/b_2	260	0.2	$b_{\text{r,5}}$	1420	0.2
c_2	400	0.2	PL	**N/A**	1.2 $\times$0.15
d_2	375	0.2	SL	**N/A**	1.2 0$\times$0.15
a_3/b_3	325	0.2	bar	**1650**	**N/A**
c_3	400	0.2			
d_3	370	0.2			
a_4/b_4	220	0.2			

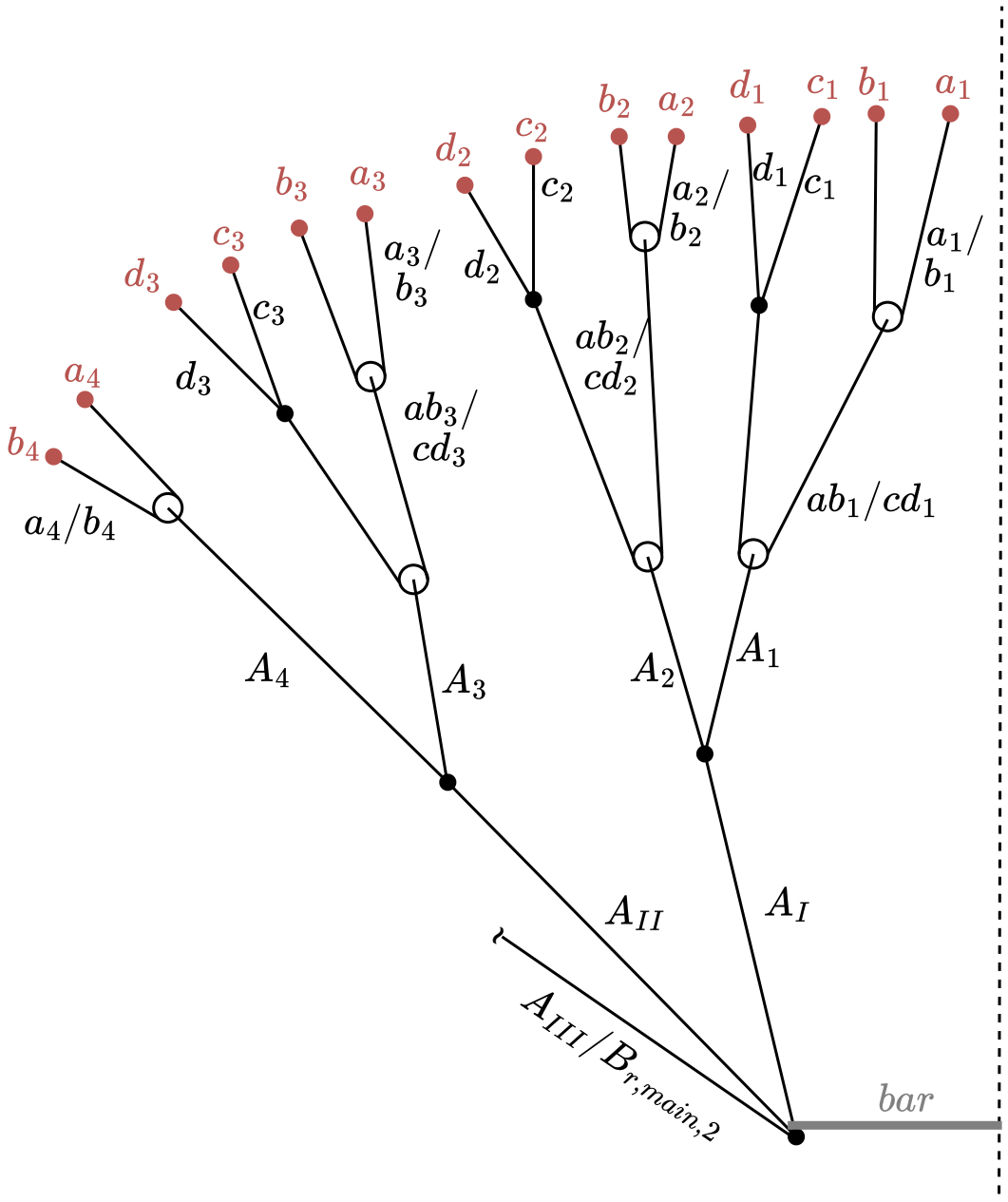

Figure B.1: Adapted V3 kite front bridle line geometry for hanging test, lengths not to scale, figure adapted from [17]

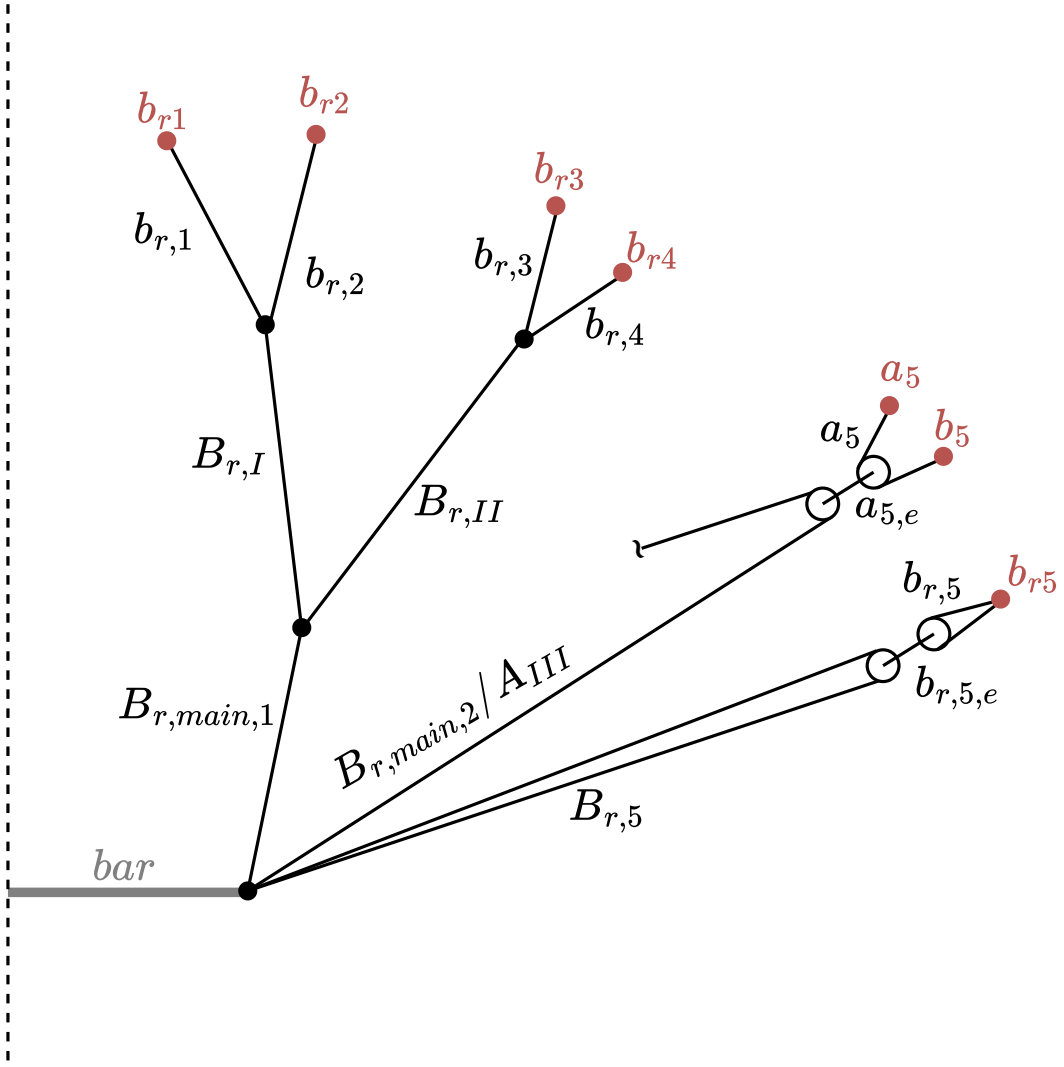

Figure B.2: Adapted V3 kite rear bridle line geometry for hanging test, lengths not to scale, figure adapted from [17]

C

Hanging test pictures

Figure C.1: Static load case 1

Figure C.2: Static load case 2

Figure C.3: Static load case 3

Figure C.4: Static load case 4

Figure C.5: Static load case 5